Université catholique de Louvain

Faculté des Sciences
Département de Physique
Institut d'Astronomie et de Géophysique Georges Lemaître

Comparing the humidity of the high troposphere as simulated by CLM with reanalysis and satellite data

Rapport de travail présenté par
Andrew Ferrone en vue de
l'obtention du diplôme d'études
approfondies en Sciences Physiques

Promoteur Pr. J. P. van Ypersele

Lecteurs Dr. M. Crucifix
Dr. B. Matthews

Année académique 2006–2007

I would like to thank J. P. VAN YPERSELE, M. CRUCIFIX *as well as* B. MATTHEWS *for their assistance throughout the academic year, and the scientific rigor they imposed on this thesis. Furthermore I would like to thank all the members of the institute for the encouragements and advices that they gave me throughout this year, as well as for the great atmosphere that is always reiging in the institute especially during lunchtime. Finally I don't want to forget my parents, who made my studies possible and thank them for their patience and encouragement.*

FOREWORD

This report gives a first evaluation of the way water vapour is simulated in the CLM model in the upper troposphere. For this task the simulated water vapour is compared to the NCEP reanalysis and satellite data from the NASA AIRS satellite. Details about this data and the comparison can be found in chapter 5.

The results presented here have been obtained in the framework of a PhD thesis which aims at evaluating the impact of aviation in Europe with a regional climate model . A motivation of this thesis as well as the importance of water vapour and especially supersaturation with respect to ice in the high troposphere is given in chapter 1 of this report.

The PhD thesis itself gives input to the climatological part of the ABCI project[1] funded by the Belgian Science Policy Office. The project aims at informing policy-makers about the environmental, political and socio-economic implications for Belgium of integrating (or not) the international aviation and maritime transport sectors into climate policy.

This reports begins with an introduction and a motivation of the work done (chapter 1) and puts this work in the framework of the PhD thesis. Chapter 2 gives a description of the properties of midlatitude cirrus clouds as these clouds play an important role in the water budget of the upper troposphere and their coverage may be altered by the presence of airplanes at these altitudes as explained in chapter 1.

A theoretical introduction into the formation of ice crystals and their properties will follow in chapter 3. A description of the regional climate model used for this report and which is also planned to be used for the PhD thesis is given in chapter 4. Finally the comparison of the model output with data from NCEP reanalysis and AIRS satellite data is made in chapter 5. The data as well as the model set up will also be explained in this chapter.

This report ends with a conclusion chapter and three annexes. Annex A gives a theoretical description of the formation of ice crystals as described in a more phenomenological way in chapter 3. Annex B gives a detailed description of the calculations and fundamental hypotheses used to derive figures about local radiative forcing impacts of aviation in Europe and Belgium. Finally annex C gives an overview of the courses followed, scientific meetings and summerschools attended during this academic year.

[1] ABC Impacts – Aviation and the Belgian Climate Policy : Analysis of Integration Options and Impacts, see http://dev.ulb.ac.be/ceese/ABC_Impacts/abc_home.php for more details

TABLE OF CONTENTS

CHAPTER I

INTRODUCTION AND MOTIVATION

This first chapter will explain why the water vapour has to be accurately simulated by the climate model, in order to be able to estimate correctly the impact of aviation on climate change in Europe.

The first section gives an overview of the way condensation trails (contrails) are formed and puts the emphasis on the importance of correct simulation of water vapour to represent the impact of contrails and aircraft induced cloudiness (AIC) on climate change. The second section compares the impact of contrails and AIC on climate on global, European, and Belgian scale, and motivates the use of a regional model for the underlying PhD thesis.

1.1 Formation of contrails

In the plume of an aircraft there is an increase in relative humidity (RH), that occurs as a result of warm, moist exhaust gases mixing with colder and less humid ambient air. RH must reach 100% during this process for contrails to appear. For climatological purposes only persistent contrails that have a lifetime of a few hours up to a day are relevant.

Figure 1 shows observations from several studies. The first one was done while contrails were clearly visible. In the second case they were at the limit of formation or disappearance, and in the third case no contrails at all were observed. Liquid and ice saturation are shown by the solid and dashed line respectively, as a function of H_2O partial vapour versus temperature.

The thin line connected to each symbol represents the mixing line of plume states between ambient and engine exit conditions (not on graph), for different types of aircrafts. The mixing process in the expanding exhaust plume is close to isobaric, that is why the mixing lines follow a linear rule in this graph, and the slope of each line is given by [**14**]:

$$\mathrm{EI(H_2O)c_p p[0.622Q(1-\eta)]^{-1}}, \tag{1}$$

where $\mathrm{EI(H_2O)}$ is the emission index of water vapour[2], c_p it the specific heat capacity of air, the ambient pressure is given by p, 0.622 represents the ratio of molar masses of water and air, and the effective specific combustion heat is given by $Q(1-\eta)$, where η is the overall efficiency of propulsion of an aircraft[3].

[2] The mass of material emitted per burnt mass of fuel

[3] Only the fraction $(1-\eta)$ of the combustion heat Q leaves the engine with the exhaust gases

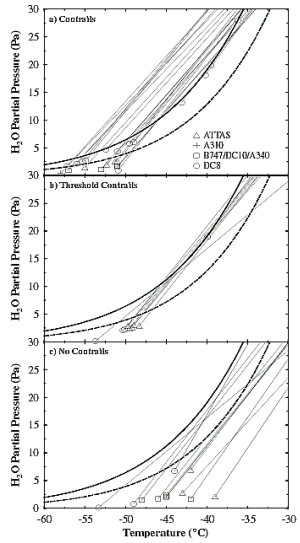

Figure 1: Water vapor partial pressure and temperature measurements and calculations from various contrail studies. Symbols indicate measured ambient conditions of temperature and H_2O abundance behind various identified aircraft. Liquid and ice saturation pressure are given by full and dashed curves, respectively. The thin line connected to each symbol represents the mixing line of plume states between ambient and engine exit conditions. (taken from [**14**])

From these graphs it can be seen that contrails exist only if the mixing line crosses or at least touches the liquid water saturation curve (The temperature needs to be low enough and enough water vapour present). This criterion is commonly referred to as Appleman-Schmidt criterion. Furthermore contrails are persistent when mixing-line endpoints fall between the liquid and the ice-saturation curves in figure 1. In this case the ambient atmosphere is supersaturated with respect to ice, and ice-particles formed in the exhaust plume of aircraft engines can grow by accumulation of water from the surrounding supersaturated air. They can evolve into cirrus clouds, and lose their line shaped appearance, thus contributing to AIC.

This shows that the model has to reproduce the temperature as well as the humidity in a reliable way at typical cruise altitudes, where contrail formation is possible due to two facts:

- These parameters are needed to verify if the Appleman-Schmidt criterion is satisfied, and thus to know if contrails are forming behind aircrafts flying in this region.
- Furthermore supersaturation has also to be simulated correctly in order to know if the contrail is going to transform into a cirrus cloud or not and thus contribute to the AIC.

1.2 Why use a regional climate model for the study of contrails?

Contrails can extend over several hundred kilometers but they are typically only a few hundred meters up to several kilometers wide [**14**]. This implies that they have a regional impact only. As the air traffic is very inhomogenously distributed on the globe, with very high concentrations over Europe and the United-States, this implies that the impact of contrails presents very strong regional variations (see figure 2).

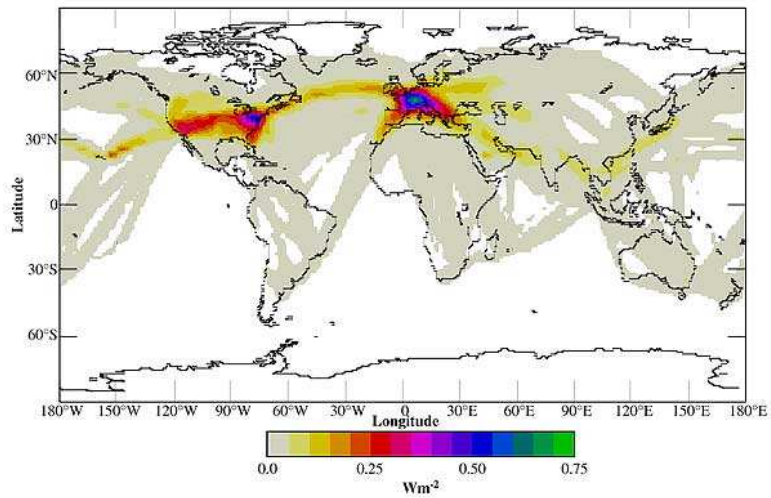

Figure 2: Global distribution of net instantaneous radiative forcing at the top of atmosphere for contrails in daily and annual average for 1992 climatic conditions and fleet. (from [**14**]).

Consequently the climate impact of aviation (due to contrails and due to ozone) is much stronger over Europe, the domain of interest of this study. Figure 3 shows the radiative forcing[4] (RF), averaged over different regions (global, Europe and Belgium) estimated within the belgian ABCI project.

In order to have an idea of the importance of the regional aspect in the computation of radiative forcing of contrails and AIC, we are now going to explain how, in the ABCI project we estimated these radiative forcing in Europe and in particular in Belgium. It is important to note that these are only preliminary results based on certain hypotheses (please refer to annex B for an extensive explanation of the different hypotheses and calculations made) that need to be confirmed in the follow up of the project. The calculations for RF of ozone is done in the following way:

$$RF_{\mathrm{O_3,EU}} = \frac{RF_{\mathrm{O_3,glo}}}{T_{\mathrm{O_3,glo}}} T_{\mathrm{O_3,EU}},$$

where $RF_{\mathrm{O_3,X}}$ indicates the radiative forcing averaged on region X, and $T_{\mathrm{O_3,X}}$ is the temperature increase due to changes in ozone concentration, as it was calculated in [**7**]. $RF_{\mathrm{O_3,glo}}$ is derived from [**33**]. On the other hand the radiative forcing of contrails and AIC, averaged over Europe (EU) or Belgium (Be), is determined as follows:

$$RF_{\mathrm{cont/AIC,EU/BE}} = \frac{Fuel\,Use_{\mathrm{EU/BE,FL>240}}}{Fuel\,Use_{\mathrm{glo,FL>240}}} \frac{Surface_{glo}}{Surface_{EU/BE}} RF_{\mathrm{cont/AIC,glo}},$$

where $RF_{\mathrm{cont/AIC,X}}$ is the radiative forcing for contrails or AIC averaged over region X, $Fuel\,Use_{\mathrm{X,FL>240}}$ is the fuel used by planes above region X and above FL240(which corresponds to 24 000ft ($\approx$ 8000m)) and $Surface_X$ represents the surface aera of the region X considered.

[4] we use the same defintion as IPCC for radiative forcing: it represents the imbalance of ingoing and outgoing radiation (expressed in $\mathrm{Wm^{-2}}$) at the tropopause holding the state of the troposphere fixed and letting the stratosphere adjust to the forcing

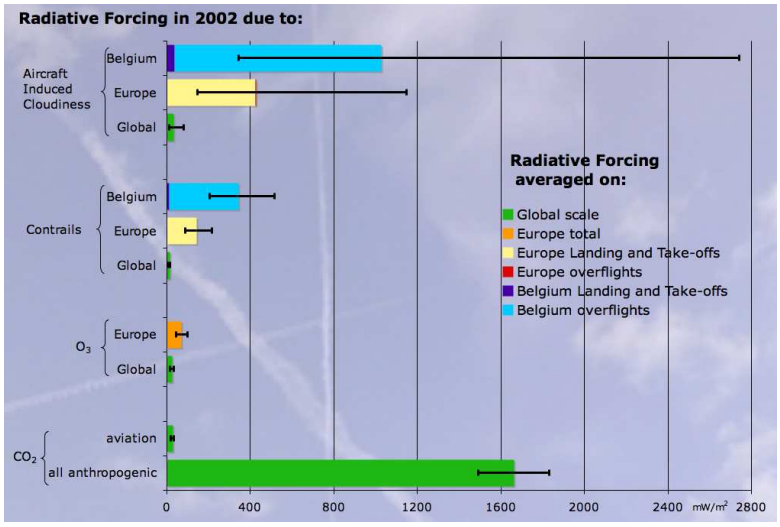

Figure 3: Relative importance of radiative forcing induced by the aviation sector (CO_2, O_3, contrails and AIC) in the year 2002 as well as radiative forcing of CO_2 from all anthropogenic sources. Where applicable the radiative forcing are averaged on different regions and a distinction is made between planes landing and taking off in the region of interest and those overflying it. Computed using [**14**], [**33**], [**6**] and [**24**]

The $RF_{\text{cont/AIC,glo}}$ is taken from [**15**] and $FuelUse_{\text{X,FL>240}}$ is determined using the AERO2k database (see [**6**]) and data from [**24**] for the flights over Belgium.

Figure 3 gives the radiative forcing (RF) of total anthropogenic CO_2, CO_2 emitted by airplanes, the RF of ozone produced by air traffic, contrails and AIC, as well as an estimation of their likelihood range[5] (error bars) as computed by [**14**] for CO_2 and [**33**] for the other forcings. Where applicable a distinction was made between the estimates for the different regions considered.

Although this chart does only represent preliminary results it is interesting to note that the situation in Belgium is very different from that of Europe. Whereas in Europe overflights (without landing or taking off in any European airport) represent only a tiny portion of all flights (less than 1%) they represent the majority of the flights over the Belgian territory ($\approx$ 70%). This reflects in the RF of contrails and AIC produced by these flights. The impact of flights landing and taking off in Belgium represent only $\approx$ 4% of RF due to contrails or AIC as most of the flights taking off or landing in Belgium do not reach an altitude above FL240 and thus produce no contrails over Belgium [**3**].

Belgium is thus receiving important climate impacts from these flights that do not contribute to the economy of the country. It is important to note that although the RF from AIC in Belgium is of the same order of magnitude as that of all anthropogenic CO_2, this does not imply that the temperature increase will be the same, as the climate system will be able to disperse part of the impact of such a strong local forcing. This phenomenon will be investigated in more detail with the help of CLM in the research involved in the underlying PhD thesis of this report.

[5] see [**15**] for a definition of the likelihood range

CHAPTER II

MIDLATITUDE CIRRUS

As has been shown in chapter 1 the cirrus cover itself can be influenced by the formation of contrails behind airliners, and this chapter will give an overview of the main microphysical properties of cirrus clouds as they are observed in mid-latidues, and thus also over Europe. This gives an important insight into the formation of cirrus clouds and their radiative properties through which they influence climate.

2.1 Cirrus structure and types

Cirrus clouds are a type of clouds that form at low temperatures in the upper troposphere above 8 km, where the temperatures are generally below $-30°C$ and are thus always composed of ice particles. They cover about 20% of the earth surface.

The most common type of cirrus clouds occurs in layers or sheets of horizontal extent of hundreds or even thousands of kilometers. Due to the fact that their horizontal extent is much greater than the vertical one they are called *cirrostratus*. Cirrus clouds can also have a patched or tufted shape, in which case they are called *cirrocumulus*. This happens when the ice crystals that form the cloud have an appreciable fall velocity so that trails of considerable extent are forming. These trails can curve irregularly, slant and sometimes form comma-like shapes. This curving is due to changes in the vertical wind velocity while the ice crystals are falling.

A last type of natural cirrus cloud is the so-called *anvil* that forms on top of a cumulonimbus and which consists essentially of ice debris which spread outward from the convective part of the storm[6]. Anvils do not include the white, dense portion of thunderstorms or the active convective column. This type of cirrus can persist even when the thunderstorm has died away and spread out to form large, widespread cloud layers. In the tropics most cirrus clouds are thought to arise primarily from cumulonimbus clouds, but this type of storms also add significantly to the cirrus clouds cover in the summer season in the mid-latitudes.

Contrails are also a type of cirrus cloud, but they are anthropogenic. Their formation process and their formation conditions were described in section 1.1.

[6]This shows that deep convection needs also to be correctly simulated by a climate model, in oder to assess the impact of cirrus clouds on climate

2.2 Cirrus particle shapes

Results in this and the following sections are based mainly on in situ measurements campaigns. Cirrus measurement campaigns conducted over Europe contain mainly: European Cloud and Radiation Experiment (EUCREX: [**29**]), the International Cirrus Experiment ICE and pre-ICE (e.g. [**26**], [**30**], [**19**]) and observations of young cirrus over Southern Germany [**19**].

The particle shape of the ice crystals that form cirrus clouds depend on the temperature at which the cirrus are formed but also on the way they are formed. Observations from [**12**] showed that for all cirrus clouds ice crystals in the form of hollow columns and hexagonal plates dominated near the cloud top. This is the part of the cloud where the crystals are formed and thus conditions are close to water saturation (after they are formed the crystals begin to fall until they reach a level were the temperature is high enough or the water content of the air low enough to melt the crystals) (see section 2.6). For the other part of cirrus clouds Heymsfeld and Platt [**12**] distinguished three temperature ranges:

- above $-40°$C spatial crystals (like bullet rosettes) are predominant (compare section 3.2.5 for description of types of ice crystals);
- between $-40°$C and $-50°$C convective cirrus contain predominantly spatial crystal forms, whereas stable cirrus contain predominately hollow columns;
- below $-50°$C hollow and solid columns predominate.

2.3 Size distribution

The form together with the size of the ice crystals play an important role in giving the extinction coefficient, an important parameter to determine the radiative properties of cirrus clouds. Although measuring the size distribution of ice crystals in cirrus clouds by in situ measurements presents some challenges (see [**23**]), because the size varies from 10-100 μm up to 1 mm, the following, general observations can be obtained from these measurements.

At low temperatures crystals are smaller than at high temperatures, due to variation of saturation water vapour with temperature. This phenomenon is increased by the fact that larger particles fall faster than smaller ones, depleting the larger particles at lower temperatures and falling into regions of the atmosphere where temperatures are higher.

In midlatitudes number concentrations have been observed to decrease exponentially with increasing size and the exponential slope of the size distribution steepens with decreasing temperature [**12**], meaning that there are fewer of the larger ice crystals at higher temperatures[7]. As already mentioned the size range stretches from above 1 mm when the temperature is above $-40°$C down to 10-100 μm when the temperature is below $-60°$C. Figure 4 illustrates this exponential decrease behavior giving dimensions of particles at different temperatures as measured by different research projects.

2.4 Extinction coefficients

In order to know the clouds radiative properties, the extinction coefficient must be known, as it gives the optical depth of the cirrus cloud when integrated over the depth of the cloud. Figure 5 shows the extinction coefficients as determined by different projects and for different temperatures. Although the results show a high scatter especially for different campaigns, which is related to different measurements techniques and different types of cirrus, Lynch et al. [**23**]

[7] This implies that as the ice crystals grow, their number is decreasing due to the fact that different crystals aggregate together as they are falling (see section 3.2.7)

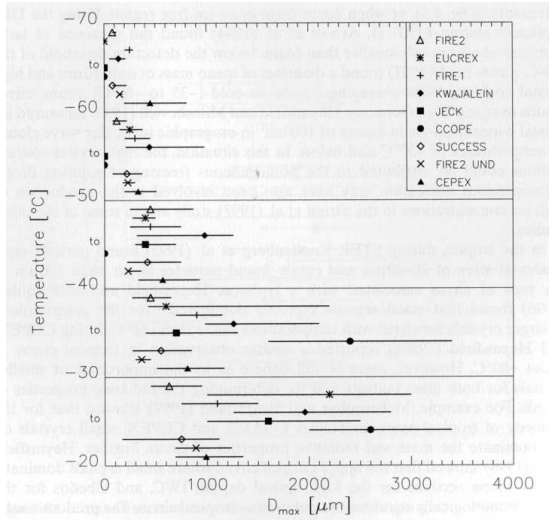

Figure 4: Maximum-detected particle size as a function of of temperature. Symbols and horizontal bars represent median values and quartiles of distributions, respectively. Data obtained from optical probes and replicators. (from [**23**])

claimed that a trend increasing σ_{ext} towards higher temperatures [8] (note the logarithmic scale) can be observed, which is in accordance with case-by-case studies that were performed by [**11**]. However this trend is not easy to recognize on figure 5, which shows that it is not easy to deduce a behavior of σ_{ext} for cirrus clouds that can be used in climate models.

2.5 Ice water content

Figure 6 shows us a similar graph as for the previous section, where ice water content of cirrus clouds is reported for different measurement campaigns and varying with temperature. For reference liquid water content in stratus clouds is typically in the range of 0.1 to 0.3 gm^{-3}.

As the diameter is decreasing with decreasing temperature we expect the same to happen to ice water content, as particles grow when they fall from the top, where they are formed, to the base of the cloud. Again the scatter between the different campaigns is quite large but the trend is discernible in figure 6 . We can observe a range from 0.1 gm^{-3} around above-30°C down to 10^{-4} gm^{-3} below -60°C. The largest ice contents are observed in anvils associated with thunderstorms due to the high vertical velocities in these convective clouds.

2.6 Three-layer cirrus conceptual model

From the previous observations and from airborne and balloon-borne measurements during the FIRE I and FIRE II projects, we may conclude that the average ice crystal size increases from cloud top downward to near cloud base, where they abruptly decrease to form cloud base.

This suggests the following formations and development mechanisms for in-situ formed ice crystals [**23**] in an idealized cirrus cloud represented by three different vertical layers[9] :

[8] This implies that it is rather the bottom of the cloud (that is at higher temperatures than cloud top) that absorbs and scatters most of the radiation

[9] In general it will be difficult to implement such a detailed representation in climate models as the cirrus

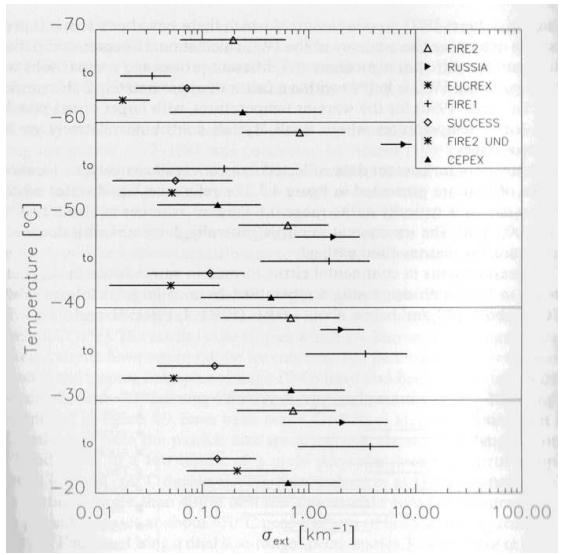

Figure 5: Volume extinction coefficient as function of temperature. Symbols and horizontal bars represent median values and quartiles of distributions, respectively. (from [**23**])

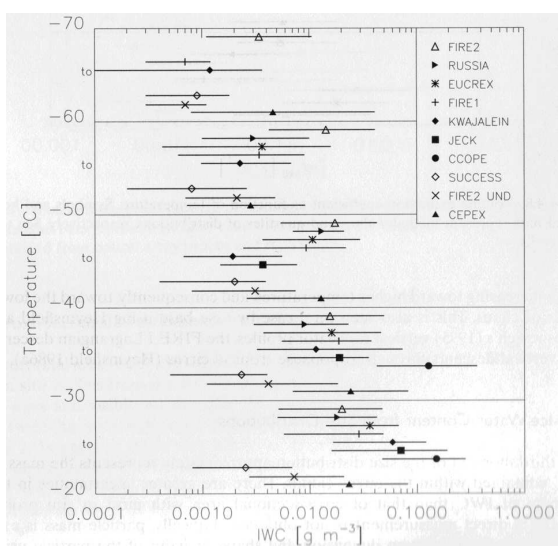

Figure 6: Ice water content as a function of temperature for different projects. Symbols and horizontal bars represent median values and quartiles of distributions, respectively. (from [**23**])

- In the uppermost layer of the cloud (layer 1) the relative humidity exceeds the relative humidity needed for ice initiation (depending on the type and numbers of ice condensation nuclei present (see 3.2.3) and nucleation processes thus forming small ice crystals. This nucleation processes will be either discrete or continuous, depending on the vertical velocities and temperatures.
- These ice crystals begin to fall into the thicker second layer, where they grow in the ice-supersaturated air. In this region ice crystals are growing from tens of microns to hundreds and even thousands of microns (see 2.3).
- Finally they reach the third thinner layer of the idealized cirrus cloud, where ice subsaturation leads to the sublimation of the ice crystals, which take an indescript shape in this final layer. In this layer the crystals created above fall into dry air, lowering the cloud base and moistening the air below. The thickness of this layer depends on the particle sizes of the crystals when they fall out of layer 2 and the relative humidity and temperature profiles in layer 3.

Only stable cirrus (that are neither forming nor disappearing) will have these three layers. It is clear that cirrus that are newly forming will not have a sublimation layer, whereas cirrus that are disappearing will not have a nucleation layer.

clouds are very thin and the vertical resolution of the model is not high enough. However this conceptual model can be used to investigate the limitations of evaluating the impacts of cirrus clouds on climate with climate models (see section 4.4.1)

CHAPTER III
Description of ICE PARTICLE GROWTH

Before giving a description of how ice clouds are modeled in the CLM climate model, an overview of the theory behind the formation of ice particles in the atmosphere is given in this chapter. It describes the different particles and interactions involved in the formation of ice crystals. This chapter is more descriptive, whereas the mathematical treatments of the different processes involved is shown in annex A.

This chapter is about ice particles that are growing in any type of cloud (not only cirrus clouds). This is done in order to give a complete overview of the microphysics involved in the formation of ice particles in the atmosphere and that is later needed for the parametrisation used in the regional climate model. Until section 3.2.4 emphasis put on the processes occurring in cirrus clouds.

3.1 Supersaturated drops

Drops[10] grow due to deposition of water vapour and by auto-conversion processes. These processes however are not sufficient to explain the formation of rain drops. Indeed in order to disturb the equilibrium between the gravitational force and the Archimedes force that applies to the drop suspended in the air, the drop has to have a certain density[11] . Knowing the density of air at a given altitude, we can thus calculate the minimal size a drop has to acquire in order to begin to fall and transform into a rain droplet.

On the other hand, as is shown in annex A, the proportionate relationship between the mass of a drop M (and its size R) and the ratio of saturation S is given by:

$$\frac{\mathrm{dR}}{\mathrm{dt}} \propto R^{-2}\frac{\mathrm{dM}}{\mathrm{dt}} \propto R^{-1}(S-1).$$

Following this relation, the growing rate of the particle is greater the smaller the initial drop size. Results from different models suggest that growth by deposition leads to a narrow size distribution (approximately 10 μm). This size is however still too small to counteract the

[10] In this chapter the term *drops* designates water that is formed via heterogeneous nucleation around condensation nuclei.

[11] The drops are supposed to form around condensation nuclei, whose density is lower than that of air (as they are suspended in the air). When water vapour is condensed on these particles their density is growing until the equilibrium between the gravitational force and the Archimedes force is broken

Archimedes force, and thus there must exist another mechanism by which the drops can grow: this is the autoconversion process. (see section 3.2.7)

3.2 Formation of ice crystals

In order to understand the way ice crystals are formed in the high troposphere we have first to describe the competition existing between the different cloud particles that trigger the formation of a cloud.

3.2.1 Homogeneous nucleation

Homogenous nucleation does not only describe the direct deposition of water vapour content, but also the possibility that the cloud, which is saturated with cloud drops in superfusion freezes instantly. Theoretic models and observations show that the rate of homogenous freezing grows from $10^{-8}\text{cm}^{-3}\text{s}^{-1}$ at $-30°\text{C}$ to $10^{13}\text{cm}^{-3}\text{s}^{-1}$ at $-40°\text{C}$. [**16**]. This implies that homogenous freezing is clearly an important process in the formation of cirrus clouds, where typical temperatures are around $-35°\text{C}$. However it will not be the only way of forming ice in high altitude clouds (compare section 2.6), this is why we will also describe the other ways of forming ice in clouds.

3.2.2 Heterogeneous nucleation

If the number of particles for ice deposition, are numerous enough at high altitudes, the ice particles can also be formed via heterogeneous processes. This type of formation processes regroups not only the interaction between the active freezing nuclei, but also the interaction with superfreezed cloud droplets.

The freezing nuclei are less numerous in the atmosphere than condensation nuclei. Moreover the complexity of heterogeneous freezing compared to condensation, is due to the fact that activity of freezing nuclei does not only depend on the rate of supersaturation but also and mainly, on the temperature of the air, which explains why they are only activated at very low temperatures.

Heterogeneous nucleation thus is composed of four possible processes:

- Depositional nucleation: water vapour is directly absorbed by the surface where is transformed into ice;
- Condensation-freezing nucleation: first, a layer of liquid water forms on the surface of the particles, that freezes in the process;
- Immersion-congelation nucleation: superfused droplets freeze instantaneously when there is a particle that penetrates in the droplet;
- Nucleation by contact: the particle freezes by contact with a freezing nuclei.

3.2.3 How a cloud is formed

The ice particles emerge either from the supersaturated drops or directly from water vapour which is contained in the air. This can occurs by *heterogeneous* or *homogeneous* nucleation as we have seen.

In order to know if water vapour is the biggest source of ice crystals in the air, we are going to describe the formation of a cloud at temperatures below the freezing point (i.e. 0°C).

The saturation pressure with respect to ice is always lower than the same saturation pressure with respect to water. We would thus expect a first level of saturation with respect to ice, would be filled with ice crystals. However in the atmosphere this is not the case. Observations show that it is only when the water vapour reaches the saturation pressure with respect to liquid water, that cloud superfusioned cloud droplets form and a cloud is arising. This thermodynamic disequilibrium is the main factor for the Bergeron process (see section 3.2.4).

The fact that the clouds only forms when the water vapour reaches the saturation pressure with respect to water, is due to three facts:

- homogeneous nucleation is only accruing at relatively low temperature.
- so called *freezing* nuclei, which help in the heterogeneous process of ice crystal formation are present in a much lower number in the atmosphere than the nuclei used for condensation of water vapour.
- Finally, the activity of the freezing nuclei is not only dependent on the humidity of the air but also on its temperature: The lower the temperature the more and smaller ice crystals are present, whereas at temperature where ice crystals are formed via heterogeneous process (i.e between 0°C and ≈ -35°C), ice crystals produced are not very numerous but quite voluminous.

This implies that the the nucleation of ice, done via a homogenous or a heterogeneous process, is less effective than the production of water droplets at temperatures and humidities of typical mid-altitude clouds. [**17**]. Generally we may thus say that clouds are first formed via the formation of liquid content, which then gets solid to form ice crystals.

3.2.4 The Bergeron process

As mentioned in section 3.2.3 clouds that are formed below the freezing point, present two levels of saturation: one with respect to ice, which is virtually empty for all types of clouds apart for cirrus clouds, and a second one with respect to water, populated by droplets in superfusion. Some of these droplets crystalize and a thermodynamic desequilibrium is appearing.

While more and more drops are being transformed into crystals, due to the action of the condensation nuclei, water vapour is not contributing any more to the growing of these droplets, but the deposition process is continuing for the crystals. This process is commonly designated as *Bergeron process*.

3.2.5 Different forms of ice crystals

Seeing the complex nature of the interactions that exist between the state of nucleation and precipitation, the different modes of growing are studied in laboratory by recreating the conditions that exist during the formation of a cloud.

These experiments show that the crystals can have four different forms and the best way is to classify these different forms following the temperature at which they have been nucleated. While these temperatures go down, we observe the formation of[12]:

- crystals in form of plates for $0°\mathrm{C} < \mathrm{T} < -4°\mathrm{C}$;
- crystals in the form of columns for $-10°\mathrm{C} < \mathrm{T} < -4°\mathrm{C}$;
- plates again for $-22.5°\mathrm{C} < \mathrm{T} < -10°\mathrm{C}$;

[12]This list is about crystals forming in all sort of clouds, not only cirrus clouds as the list in section 2.2

- finally, crystals in form of columns and plates for $T < -22.5°C$.

Figure 7 gives an overview of these different forms of ice crystals that are formed.

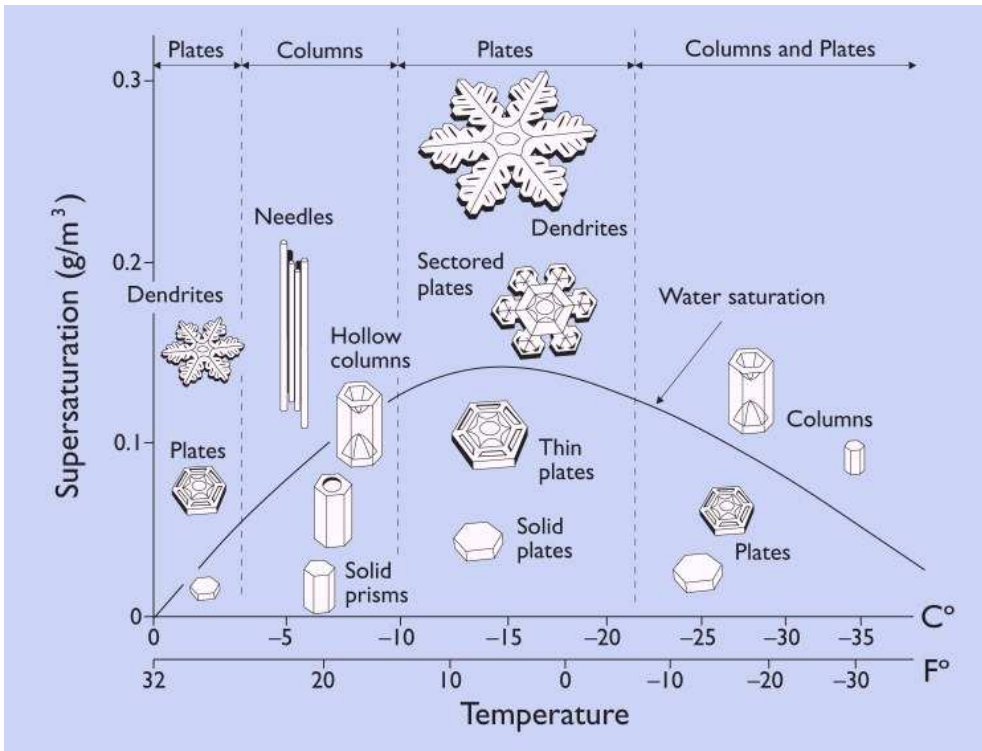

Figure 7: Forms of ice crystals at different temperature of nucleation process (source: http://www.its.caltech.edu/ atomic/snowcrystals/)

After the ice crystals are formed in an initial step, they continue growing and by this process they are trying to reproduce the hexagonal crystalline structure. The way they do it will not only depend on the deposition of water vapour but also of the orientation of the surface with respect to the hexagonal grid, that exists in its proper structure. If the deposition rate is relatively slow, the crystals are simply growing following its original form, plane or elongated. However as the depositional growth becomes greater the ice crystals in the form of needles continue to grow, whereas the plates lead to the well known dendrites (see figure 8). As can be seen on this picture the structure grows by the branches of the dendrite. This is due to the fact that the saturation vapour pressure is greater around the spikes of the dendrite than the faces due to the geometry of the structure. At this point we may remark that it is very rare to encounter perfect symmetrical ice crystals in the natural environment, as the water vapour is not perfectly isotropic at these scales.

3.2.6 Ice crystal growth by rimming

The process of *rimming* is often mentioned in the literature and designates the collection of water droplets by the ice or snow crystals, or more in general the collection by ice crystals of any liquid (i.e water droplets or rain)(see picture 9).

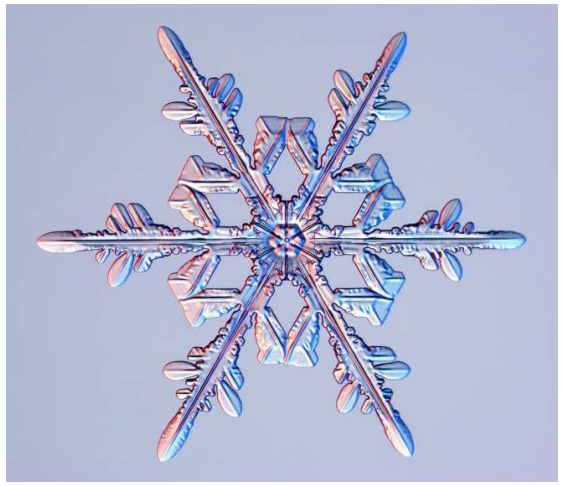

Figure 8: Example of a symmetrical dendrite grown in laboratory (source: http://www.its.caltech.edu/ atomic/snowcrystals/)

This is one of the most important processes in the formation of snow and hail. For the process to get started ice crystals need to have a certain size: the minim size for plane ice crystals is around 100μm, whereas it is around 50μm for elongates ice crystals.

In order to quantify this process we need to evaluate the probability of collision between water and ice particles, falling at different velocities. This can be represented by considering a cylinder that is traversed by time unit and the area of its base is given by πR^2, where R is the radius of the biggest particle entering in collision with the smaller one.

The terminal velocity of the more massive particle of the two is given by:

$$U_T = \sqrt{\frac{4\rho_i g}{3\rho c_D}} R,$$

where ρ_i is the density of the particle, ρ is the density of the air, c_D is the viscosity coefficient, and g is the acceleration of gravity.

We will assume that the velocity of the particle that is collected is zero. The volume traversed per unit of time is equal to $\pi R^2 U_T$. If the air in this volume contains particles with radius r_i, then the total mass of particles in the considered volume is given by:

$$\chi = 4/3\pi\rho_l \sum_i N_i r_i^3,$$

where ρ_l is the type density of the small particles in the volume and N_i is their number per unit of volume.

The rate of growth of the particle by accretion is given by:

$$\frac{\mathrm{dM}}{\mathrm{dt}} = \frac{\mathrm{dM}}{\mathrm{dR}}\frac{\mathrm{dR}}{\mathrm{dt}} = \frac{U_T \chi E_1 E_2}{4\rho_l}$$

where E_1 is the efficiency factor an gives the probability of collision between the particles and E_2 is the factor of coalescence and gives the probability that a particle that two particles entering into collision stay effectively together. Both of these factors depend of the form and

Figure 9: Example of dendrite completely covered with rime, but you can still see the six-fold symmetry of the underlying stellar crystal (source: http://www.its.caltech.edu/ atomic/snowcrystals/)

the relative velocity between the particles. The coalescence factor E_2 depends moreover on the temperature and humidity condition on the surface of the particle.

The efficiency factor is bigger for higher relative speeds, because in this case the aerodynamic flee phenomena is less important than at low speeds.

The growing by rimming is more effective than the growing by deposition. In both cases the crystal is falling faster and faster as is becomes more heavy. In the case of deposition this is done more or less homogeneously, and thus the drag increases. However in the case of rimming the accretion of material follows more or less in the same direction than the fall direction and the drag stays more or less the same. We thus conclude that the importance of rimming for a falling ice crystal becomes more and more important as it is approaching the 0°C isotherm.

3.2.7 Autoconversion and aggregation of ice crystals

Finally we would like to mention the autoconversion process which designates the natural tendency of ice crystals to form aggregations between themselves during the nucleation process (due to the fact that they begin to fall) This leads then to the formation of snow if the diameter of the aggregates is big enough.

On the other side, when the air is sufficiently turbulent, the ice crystals can enter in collision with one another and they coagulate between them. This is another way of forming snow particles and is generally designated as aggregation process.

CHAPTER IV

The Climate Version of the 'LOKAL MODELL'

In this section we are going to give an overview of the way the climate version of the *Lokal Modell* (CLM) is working. This model is derived from the operational meteorological model used by the *Deutscher Wetterdienst* (DWD). The main difference between the meteorological model and the climate version are to be found in the soil model (TERRA_ML), which is much more detailed in the climate model in order to be able to permit longer simulation runs[13]. It contains 10 soil layers, with vertical homogenous soil types up to a depth of 15 m.

The model is designed to do long, nested simulation of 1 to 100 years at high spatial resolution (50 to 2 km) and can be forced by GCM (General Circulation Models) simulations or operational analysis and reanalysis.

We have decided to use this model after a first global comparison of ten different models available. The comparison was based on scientific aspects, in particular the parametrisation of the microphysics of clouds was considered as well as the validation of the model for the European climate. Also other aspects such as the availability of the model code and the importance of the user group were considered.

Out of this first selection three models were investigated in more detail during this first thesis year: MAR, RegCM3 and CLM.

MAR (Modèle Atmosphérique Régional) is a model that was developed at the ASTR institute. It includes an explicit parametrisation of the microphysics of ice clouds. Its main drawbacks are that the model is not yet fully validated for European climate as well as the fact that the user group is reduced. Moreover the model is not written to be run on several CPUs in parallel (thus reducing the time needed for a numeric experiment).

RegCM3 is derived from the global climate model HadCM3 developed by the British Meteorological Office, which is a model widely used and also one of the models used for the latest IPCC report. The microphysical parametrisation is simpler than the parametrisation of MAR and CLM, but was judged to be sufficient for the work. The main drawback of the model is the fact that it is not developed anymore (a new version exists but it was not possible to access the code of this new version) and thus new developments, that can be made during this PhD thesis will not be included in the official version of the model. After some time trying to run

[13]The soil model is needed in order to get proper fluxes of radiation and water at the boundary between the atmosphere and the surface. CLM does not include an ocean model and the ocean state is prescribed by the forcing of the model (and is varying in time). This input is sufficient to derive the fluxes between the ocean and the atmosphere in a regional climate model.

the model we did not succeed to get the model to run on our machines at the institute, which led to us to abandon this model.

Finally CLM was chosen based on the fact that microphysical cloud parametrisation is very explicit and the model is validated for present European climate and the validation for future climate is in progress. The other advantages are that the model is quite new and thus development is still in progress and new insights can be included in the model. Moreover the model has a quite large international user group (although not as large as RegCM3). Its main drawback is that the model is very CPU intensive (mainly due to the fact that the hydrostatic approximation is not used), but this is partly compensated by the fact that the code is written so that the model can be run on several CPUs.

4.1 Model overview

One of the main differences between CLM and other regional climate models (e.g. RegCM3, MM5, Aladin[14]) is that it does not rely on the hydrostatic approximation. This allows the model to be used on the meso-β and meso-γ scale[15]. In operational meteorological forecasts the model is employed down to 1 to 3 km grid spacing, which permits an explicit resolution of deep convection[16].

The atmospheric part of the model is based on the primitive thermo-hydrodynamical equations in advection form that describe a compressible flow in a moist atmosphere. These equations are solved on a terrain-following height coordinate with rotated geographical coordinates and user defined stretching in the vertical. The resolution of the equations is done using a second-order leapfrog time split integration scheme (HE-VI, explicit in horizontal directions and implicit in the vertical direction).

The boundary conditions for the wind field, the temperature, the pressure and the sea surface temperature (on the lower boundary of the domain) are imposed via Davies lateral conditions [**2**]. The top of the model is situated at 20 hPa, where Rayleigh damping is performed and the rigid lid approximation applies. Moreover the vertically integrated ozone, the leaf area index, plant cover as well as temperature and water content of deep soil are prescribed.

Subgrid physical processes are taken into account by a variety of parametrisation schemes. These include:

- Subgrid-scale turbulence; vertical turbulent fluxes are calculated by a diagnostic second order K-closure scheme.
- Surface layer parametrisation: Momentum is derived from a stability-dependent drag-law formulation and fluxes of heat and moisture are based on the similarity theory [**22**].
- Grid-scale clouds and precipitation, this scheme is based on cloud water condensation and evapouration by saturation adjustment. This scheme will be described in more detail in section 4.2.
- Subgrid-scale clouds cloudiness is based on a Gaussian distribution of saturation deficit, whose standard deviation is empirically determined and is described in section 4.3.
- Moist convection is based on a scheme by [**35**], based on mass-flux convection with equilibrium closure.

[14] http://www.mi.uni-hamburg.de/Mesoscale-meteorology-models.675.0.html gives an overview over different mesoscale meteorology and climate models

[15] These are different meteorological scales: The Meso-γ scale (2-20 km), deals with phenomena like thunderstorm convection, complex terrain flows, whereas the Meso-β scale (20-200 km) deals with phenomena like sea breezes, lake effect snow storms

[16] The model includes a convection parametrisation that can be switched on to run the model at lower resolution

- Radiation is parametrised by a δ two-stream radiation scheme after Ritter and Geleyn [**31**], which includes full cloud-radiation feedback (see section 4.4).

4.2 Grid-scale clouds and precipitation scheme

After this general overview of the model structure we are now going to concentrate on the parametrisation of micro-physical cloud quantities, which will lead to the formulation of super-saturation with respect to ice in the model and to the radiation properties of clouds, in particular those of cirus clouds formed by ice particles.

In the two-categories ice scheme cloud ice, assumed to be in the form of small hexagonal[17] plates that are suspended in the air, and snow, in the form of rimmed aggregates of ice-crystals, that are large enough to have an appreciable fall velocity, are included together with the liquid phase, composed of cloud water and rain.

The growth of ice-crystals is a non-equilibrium process in the model and requires at all temperatures saturation with respect to water. This assumption leads to two issues. First this requires that the whole grid cell has to saturated before clouds are formed, which presents certain problems, compare section 4.3 and chapter 5. Secondly as has been noted in section 3.2.3 some ice crystals can form when the water vapour reaches saturation with respect to ice, although their number is very limited. The assumption that not a single crystal from below saturation with respect to water should lead to a small underestimation of cloudiness.

The treatment of ice crystals in the model requires assumptions on the shape, number and density of crystals. A monodisperse distribution for cloud ice is assumed with a mean crystal mass given by:

$$q_i = \rho q_i N_i^{-1}, \tag{2}$$

where ρ is the total density of the air, q_i is the mass fraction of ice crystals and N_i is the number of cloud ice particles per unit volume of air. ρ is calculated in the resolution of the dynamic equations of the model and q_i is predicted as part of the moist convection scheme, thus we need to specify N_i. This quantity is approximated by a relation derived from aircraft measurements of concentration of pristine crystals in stratiform clouds using data of [**13**] and [**25**]:

$$N_i(T) = N_0^i \exp[0.2(T_0 - T)], \tag{3}$$

were $N_0^i = 1.0 \cdot 10^2 \mathrm{m}^{-3}$ is the average concentration at $T = T_0$, and T_0 is the freezing point temperature of water. The experimental data may scatter by about two order of magnitudes around the value given by (3) for a given temperature.

Knowing the mean crystal mass (q_i) we can immediately determine the dimension of the crystals, which are assumed to be hexagonal plates with a diameter D_i and thickness h_i. If the diameter is smaller than 220 μm and have been measured to be up to 1mm in diameter(see section 2.3) the aspect ratio can be considered to be constant. $h/D_i = 0.2$. Assuming an ice density of $5 \cdot 10^2$ kg m^{-3} the diameter of the ice crystals is given by:

$$D_i = \sqrt[3]{\frac{q_i}{a_m^i}},$$

where $a_m^i = 130$ kg m^{-3}, is the form factor approximated to be independent of the temperature[18].

[17] This is a simplified view of the different forms on ice crystals in nature, see section 3.2.5

[18] As was explained in chapter 2, ice crystals have different shapes depending on the temperature at which they form (see section 2.6)

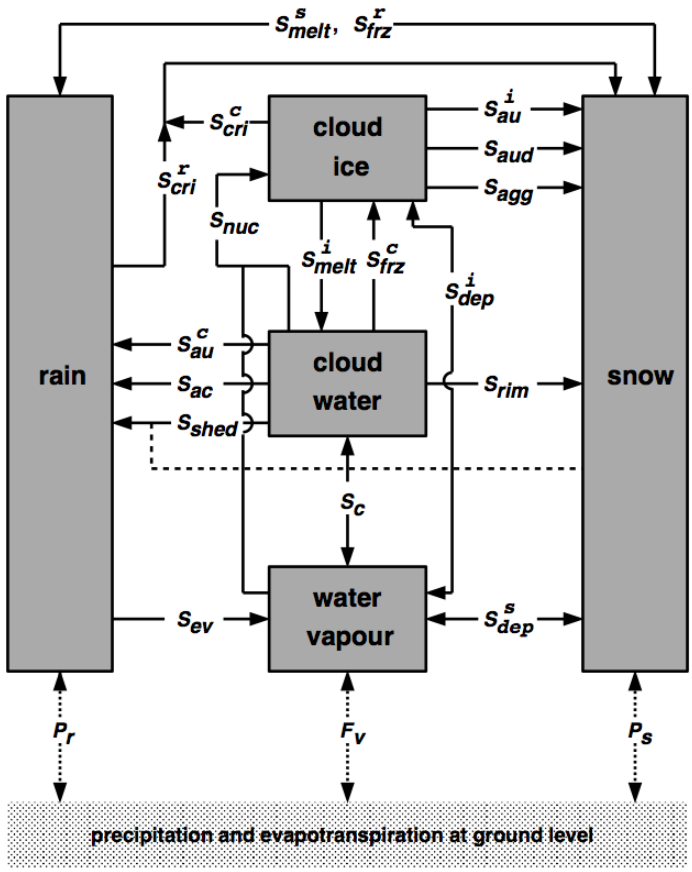

Figure 10: Transfer between different states of water in the atmosphere as they are parametrised by the precipitation scheme (taken from the scientific documentation of the LM model, http://cosmo-model.cscs.ch/public/downloads/scientificDoc.zip)

The transfer modes between the different states of water in the atmosphere in the model are shown in figure 10 and are approximated by integration of individual particle growth rate.

In the next sections we are going to concentrate first on the rate of formation of cloud ice, and then on the rate of its removal. However it is important to note that the transfer rate of cloud water condensation S_c obtained by saturation adjustment implies that high supersaturation with respect to ice is possible and implies a fast quick deposition of ice water on the crystals.

4.2.1 Growth of cloud ice

This section will describe the growth of cloud ice by nucleation, homogenous freezing and depositional growth.

For the heterogeneous nucleation the number of ice forming nuclei within a time step Δt is given by equation (3) and there is no distinction between the different nucleation processes. Moreover no nucleation is supposed to occur whenever ice is already present, as these contributions have been found to be of minor importance (compare to section A.3). The transfer rate

due to nucleation is thus given by:

$$S_{nuc} = \begin{cases} \frac{1}{\rho}\frac{q_i^0}{\Delta t}N_i(T) & \text{if } T < T_d, \quad q_i = 0 \quad \text{and } q^v \geq q_{si}^v, \\ \frac{1}{\rho}\frac{q_i^0}{\Delta t}N_i(T) & \text{if } T_d \leq T \leq T_{nuc}, \quad q_i = 0 \quad \text{and } q^v \geq q_{sw}^v, \\ 0 & \text{else.} \end{cases} \tag{4}$$

where $q_i^0 = 10^{-12}$kg is the initial mass of the ice crystals, $T_d = 248.15$K and $T_{nuc} = 267.15$K are threshold temperatures. q_v is the water vapour of the atmosphere, q_{si}^v is the saturation specific humidity with respect to ice and q_{sw}^v is the same quantity with respect to water. The calculation of these saturation values is specified in section 4.2.3.

The other way by which cloud ice is formed is via homogenous freezing of supercooled cloud droplets. As described in section A.2 it is not possible to represent explicitly the homogeneous nucleation process in models, thus the ice cloud parametrisation scheme assumes that all cloud water freezes instantaneously whenever the temperature falls below a threshold temperature $T_{hn} = 236.15$ K. The rate of homogenous nucleation is then given by:

$$S_{frz}^c = \begin{cases} q^c/\Delta t & \text{if } T < T_{hn} \text{ and } q^c > 0, \\ 0 & \text{else,} \end{cases} \tag{5}$$

where q^c is the mass fraction of cloud water.

Once the ice crystals are formed they will grow by vapour deposition in a non-equilibrium process. The growth equation of this process is given by a strongly simplified form of equation(16):

$$(\dot{q}_i)_{dep} = 4D_iG_id_v\rho(q^v - q_{si}^v), \tag{6}$$

for a cloud ice crystal of mass q_i with diameter D_i. d_v is the diffusion coefficient for water vapour which is calculated by the model, q^v is the specific humidity, q_{si}^v is the saturation specific humidity, and ρ is the density of water. The factor G_i is calculated from the Howell factor H_i: $G_i = 1/(1 + H_i)$. H_i, which is given by:

$$H_i = \frac{d_vL_s^2}{l_hR_dT^2}\rho q_{si}^v,$$

where L_s is the latent heat of vapourization, l_h is the thermal conductivity of dry air and R_d is the gas constant for dry air.

Defining the total deposition of crystals as $S_{dep}^i = N_i\dot{q}_i/\rho$, we can thus write:

$$S_{dep}^i = 4N_iD_iG_id_v(q^v - q_{si}^v) \qquad \text{if } q^v > q_{si}^v.$$

Defining moreover $c_{dep}^i = 4G_id_v(a_m^i)^{-1/3}$, this is considered a constant in the model as the Howell factor is varying slowly with temperature and pressure and is set to $c_{dep}^i = 1.3 \cdot 10^{-5}$. Using this relation and using the mass-size relation given by $q_i = a_m^iD_i^3$ the above relation simplifies to:

$$S_{dep}^i = c_{dep}^iN_iq_i^{1/3}(q^v - q_{si}^v) \qquad \text{if } q^v > q_{si}^v.$$

The number of ice crystal in this equation is given by (3) and the mass q_i is diagnosed from q_i and N_i following relation (2).

4.2.2 Removal of cloud ice

In this section the remmoval of cloud ice via sublimation, aggregation, autoconversion and instantaneous freezing processes is described.

For cloud ice sublimation at ice subsaturation the following relation is used:

$$S^i_{dep} = \max\{-q_i/\delta t, (q^v - q^v_{si})/\delta t\} \qquad \text{if } q^v < q^v_{si}.$$

The autoconversion process of cloud ice to snow due to ice crystal aggregation is given via a linear threshold relation:

$$S^i_{au} = \max\{c^i_{au}(q_i - (q_i)_0), 0\},$$

where the conversion factor $c^i_{au} = 10^{-3}\mathrm{s}^{-1}$ and the threshold value is set to zero ($(q_i)_0 = 0$).

Snow may also be formed by fast depositional growth of small crystals. If we denote the time-scale for this process by τ_s, we can calculate this depositional growth rate to be given by: $S^d_{au} = q_i/\tau_s$. In order to to estimate τ_s we will integrate the mass growth relation equation (6) in the form $\mathrm{dq_i} = \alpha \mathrm{m}^{1/3}\mathrm{dt}$, were $\alpha = 4(a^i_m)^{-1/3}G_i d_v \rho(q^v - q^v_{si})$, which yields:

$$\tau_s = \frac{3}{2\alpha}\left\{(m^0_s)^{2/3} - (q_i)^{2/3}\right\}.$$

Putting this relation into the expression for depositional growth rate we get:

$$S^d_{au} = \frac{\alpha q_i}{1.5 q_i^{2/3}\{(m^0_s/q_i)^{2/3} - 1\}}.$$

Replacing α by its expression and using the mean crystal mass ice relation (2) this simplifies to:

$$S^d_{au} = \frac{S^i_{dep}}{1.5\{(m^0_s/q_i)^{2/3} - 1\}}.$$

For the model calculations the initial mass of snow crystals m^0_s is set to $m^0_s = 3.0 \cdot 10^{-9}$ kg.

In order to estimate the aggregation term (S_{agg}), which corresponds to the mass increase of snow due to aggregation of ice particles, we will use the mass growth equation for aggregation:

$$(\dot{m}_{agg}) = \frac{\pi}{4} D^2_s E_s(D_s) v^s_T(D_s) \rho q_i,$$

4.2.3 Calculations of saturation-specific humidity

In this section we first give the expression that is used in the model to calculate the specific humidity with respect to water:

$$q^v_{sw}(T,p) = \frac{R_d}{R_v}\frac{p^v_{sw}(T)}{p - (1 - R_d/R_v)p^v_{sw}(T)}, \tag{7}$$

where R_d and R_v are respectively the gas constants for dry air and water vapour, and $p^v_{sw}(T)$ is the equilibrium vapour pressure over a plane surface of water. This is calculated using the empirical formula given by Teten:

$$p^v_{sw}(T) = p^v_0 \exp\left(a_w \frac{T - T_r}{T - b_w}\right),$$

where the $p^v_0 = 610.78\mathrm{Pa}$, $T_r = 273.16\mathrm{K}$, $a_w = 17.27$ and $b_w = 35.86\mathrm{K}$ are parameters that are fixed so as to fit observational data.

In a similar way, the ice saturation specific humidity q^v_{si} and the equilibrium vapour pressure over a plane surface of ice are p^v_{si} are respectively given by:

$$q^v_{si}(T,p) = \frac{R_d}{R_v}\frac{p^v_{si}(T)}{p-(1-R_d/R_v)p^v_{si}(T)}, \tag{8}$$

and

$$p^v_{si}(T) = p^v_0 \exp\left(a_i \frac{T-T_r}{T-b_i}\right),$$

where $a_i = 21.875$ and $b_i = 7.66$K.

Theses values are presented as a function of altitude in the standard atmosphere in figure 11.

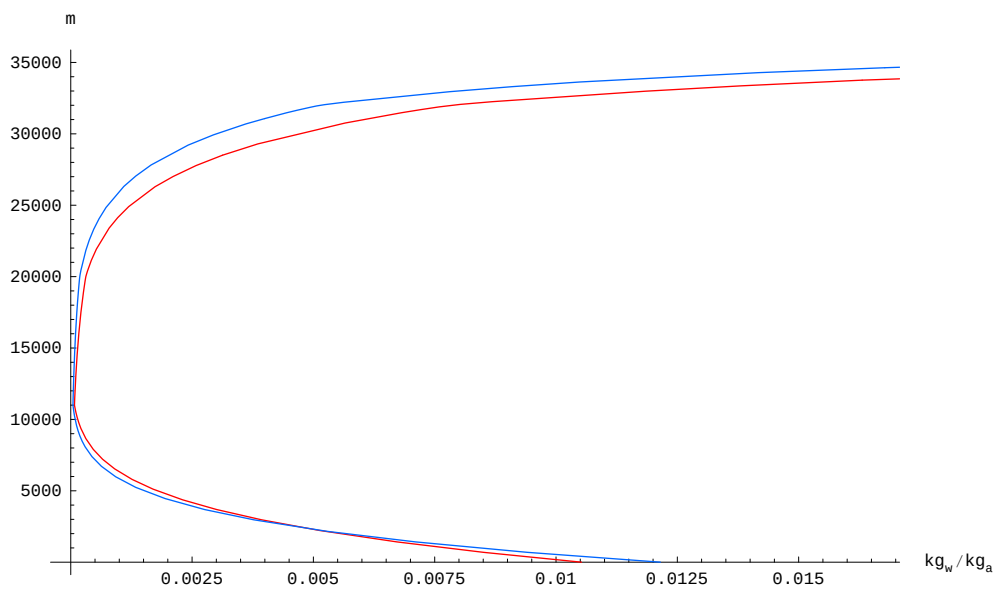

Figure 11: The saturation specific humidity over water ($q^v_{sw}(T,p)$) in red and over ice ($q^v_{si}(T,p)$) in blue as a function of the altitude in the standard atmosphere expressed in kilogram of water vapour per kilogram of air ($\mathrm{kg_w/kg_a}$)

4.3 Subgrid-scale clouds

As we have seen in the previous section the scheme of parametrisation uses saturation equilibrium for calculation of condensation rate. This implies that the whole grid cell has to reach saturation before cloud water is formed.

Clouds which are smaller than the dimensions of the grid cell are not explicitly represented by the model. Figure 12 represents this phenomenon in a schematic way. This figure shows that even though the whole grid cell is not saturated with respect to water, some parts of it are.

If the model is run at high resolution (e.g $0.16° \times 0.16°$) this is not a problem for the representation of water vapour and cloud water content. However for radiation this is not sufficient. In order to have a correct simulation of radiation processes the model has to calculate

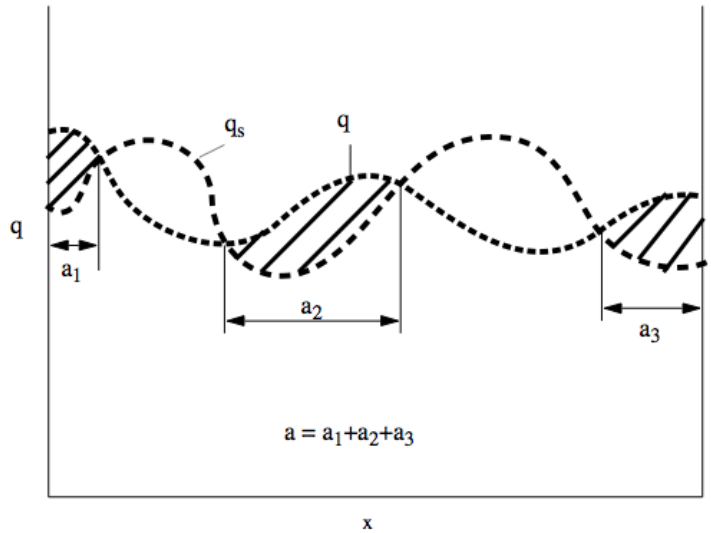

Figure 12: Schematic representation showing the existence of clouds in a one-dimensional grid cell. The small-dashed line (q) represents the variation of humidity in the grid cell, whereas the long-dashed line(q_s) represents the variation of saturation humidity in the cell. In the shaded regions where q is higher than q_s clouds exists. $a = a_1+a_2+a_2$ represents the subgrid cloudiness. (source: http://www.bom.gov.au/bmrc/basic/wksp16/papers/Jakob.pdf)

a sub-grid cloudiness (varying between 0 and 1) for each grid-cell. The way to calculate first the microphysics of the model, without taking into account subgrid-scale cloudiness and do a correction afterwards (as will be explained in this section) is at our knowledge a unique feature of CLM. This section will describe how this fractional cloudiness is calculated.

4.3.1 Calculation of partial cloudiness

A Gaussian distribution is assumed for the saturation deficit given by:

$$\mathrm{dq} = \mathrm{q_t} - \mathrm{q_s},$$

where $q_t = q_v - q_s$ is the total water content and q_s is saturation specific humidity. Using the standard deviation of this distribution and the conservative grid-scale quantities q_t and T_l (liquid water temperature), a corrected liquid water content is determined, which contains also the contributions from subgrid-scale cloudiness[19].

As the model is not capable of calculating explicitly the standard deviation (σ) of the saturation deficit (dq) it is estimated in the turbulence parametrisation of the model. The subgrid cloudiness (clc) is then estimated as:

$$clc = \begin{cases} 0 & \text{if } \mathrm{dq}/\sigma < -(\mathrm{dq}/\sigma)_{\mathrm{crit}} \\ 0.5\left(1 + \frac{\mathrm{dq}/\sigma}{(\mathrm{dq}/\sigma)_{\mathrm{crit}}}\right) & \text{if } -(\mathrm{dq}/\sigma)_{\mathrm{crit}} \leq \mathrm{dq}/\sigma \leq (\mathrm{dq}/\sigma)_{\mathrm{crit}} \\ 1 & \text{if } \mathrm{dq}/\sigma > (\mathrm{dq}/\sigma)_{\mathrm{crit}} \end{cases}$$

[19]The subgrid cloudiness, is a parameter varying from 0 to 1 and indication which part of the grid cell is covered with clouds (0, means cloud free, 1 meaning completely covered).

In CLM $(\mathrm{dq}/\sigma)_{\mathrm{crit}} = 4$. This implies that dq has to be 4 times greater/smaller than its standard deviation, so that the grid cell is fully covered with clouds/free of clouds. At saturation ($\mathrm{dq} = 0$) it is assumed that half of the grid is covered with clouds.

Moreover the parametrisation also calculates an estimation of the cloud water content based on the standard deviation of dq as follows:

$$q_l = \begin{cases} 0 & \text{if } \mathrm{dq}/\sigma < -(\mathrm{dq}/\sigma)_{\mathrm{crit}} \\ \frac{\gamma\sigma(\mathrm{dq}/\sigma+(\mathrm{dq}/\sigma)_{\mathrm{crit}})(\mathrm{dq}/\sigma+(\mathrm{dq}/\sigma)_{\mathrm{max}})}{2((\mathrm{dq}/\sigma)_{\mathrm{crit}}+(\mathrm{dq}/\sigma)_{\mathrm{max}})} & \text{if } -(\mathrm{dq}/\sigma)_{\mathrm{crit}} \leq \mathrm{dq}/\sigma \leq (\mathrm{dq}/\sigma)_{\mathrm{max}} \\ \gamma\sigma & \text{if } \mathrm{dq}/\sigma > (\mathrm{dq}/\sigma)_{\mathrm{max}} \end{cases},$$

with $(\mathrm{dq}/\sigma)_{\mathrm{max}} = (\mathrm{dq}/\sigma)_{\mathrm{crit}} \left(\frac{1}{\mathrm{clc(dq=0)}} - 1) = 4\right)$, and $\gamma = 1/\left(1 + \frac{L_s}{C_{pd}} \frac{\mathrm{dq_{sw}^v}}{\mathrm{dT}}(T_l, qs)\right)$, with L_s the latent heat of evapouration, C_{pd} the specific heat of dry air at constant pressure and T_l the liquid water temperature.

4.4 Radiation scheme including clouds

As already mentioned, the radiation scheme is based on Ritter and Geleyn [**31**]. The radiation scheme is particular important for a climate model as the interaction between clouds and radiation will have a strong impact on the surface energy, and thus on the atmospheric temperature profiles in the lower tropshere. This modified atmospheric structure will in turn affect the generation and dissipation of clouds, thus generating a strong feedback on quantities like the diurnal cycle and near-surface temperature. It is clear that the interaction between atmospheric components (gaseous components, aerosols and clouds) should be modeled as accurately as possible, without making the CPU calculation too slow.

This scheme is based on the δ-two-stream equations as described by [**37**], which can be described by the following set of equations[20]:

$$\begin{aligned} \frac{\mathrm{dF_1}}{\mathrm{d}\delta} &= \alpha_1 F_1 - \alpha_2 F_2 - \alpha_3 J \\ \frac{\mathrm{dF_2}}{\mathrm{d}\delta} &= \alpha_2 F_1 - \alpha_1 F_2 + \alpha_4 J \\ \frac{\mathrm{dS_{||}}}{\mathrm{d}\delta} &= -\frac{S_{||}}{\mu_0} \end{aligned} \tag{9}$$

which have been modified from the original equations of [**37**], so that they are more computing efficient to solve. Table 1 gives a list of the different parameters used:

Equations (9) are then solved by subdividing the atmosphere into layers of constant optical properties following [**9**]. These layers of constant optical properties are the model layers which are too thick to simulate the 3-layer model of cirrus clouds that was described in section 2.6. This problem could be solved in increasing the vertical resolution of the model at the limit of the troposphere, where cirrus clouds are forming.

4.4.1 Treatment of partial cloudiness and cloud optical properties

The partial cloudiness case is treated in CLM by characterizing for each layer two sets of optical parameters, one for the cloudy and one for the cloud-free part as introduced by [**9**]. This treatment requires to consider the relationship between the cloudy and the cloud-free part. In CLM this done via a maximum overlap of clouds in adjacent layers. Ritter and Geleyn affirm

[20] see table 1 for a list of symbols used

$$
\begin{aligned}
\alpha_1 &= U(1-\tilde{\omega}(1-\beta_0)) \quad \text{solar/infrared;} \\
\alpha_2 &= U\beta_0\tilde{\omega} \quad \text{solar/infrared;} \\
\alpha_3 &= \begin{cases} \tilde{\omega}\beta(\mu_0) & \text{solar} \\ U(1-\tilde{\omega}) & \text{infrared} \end{cases}; \\
\alpha_4 &= \begin{cases} \tilde{\omega}(1-\beta(\mu_0)) & \text{solar} \\ U(1-\tilde{\omega}) & \text{infrared} \end{cases}; \\
J &= \begin{cases} S_{||}/\mu_0 & \text{solar} \\ \pi B & \text{infrared} \end{cases}; \\
\delta &= (1-\tilde{\omega}')\delta'; \\
\tilde{\omega} &= \frac{\tilde{\omega}'(1-f)}{1-\tilde{\omega}'f}; \\
\beta_0 &= \frac{4+g}{g(1+g)}; \\
\beta(\mu_0) &= \frac{1}{2} - \frac{3}{4}\frac{g}{1+g}\mu_0;
\end{aligned}
$$

F_1, F_2	diffuse upward, downward flux;
$S_{\|\|}$	parallel solar flux with respect to a horizontal plane;
μ_0	cosine of solar zenithal angle;
δ'	optical thickness;
$\tilde{\omega}'$	single scattering albedo;
g^λ	asymmetry factor for the phase function;
f	fraction of radiation contained in the diffraction peak of the phase function;
U	diffusivity factor;
β_0	mean fractional backscattering coefficient for diffuse light;
$\beta(\mu_0)$	mean fractional upward-scattering coefficient for primary scattered solar radiation;
B	blackbody radiation.

Table 1: List of the different parameters used in the [**31**]scheme

that this method gives a better estimation of the cloud cover than the widely used random overlap, which overestimates cloud cover.

The most important parameter that has to be estimated when inteferences with clouds and radiation is estimated, is the cloud radiative forcing (CRF), defined as the impact of clouds on the actual radiative fluxes at the top of the atmosphere.

To derive spectrally averaged optical properties for the different cloud types the following condition for the droplet absorption k is used:

$$\frac{\partial}{\partial k^\lambda}\left\{\sum_{n=1}^{N} w_n(\bar{\tau}^\lambda - \exp(-\bar{k}^\lambda \Delta_n z))^2\right\} = 0,$$

where w_n represent weighting factors, that have to be determined and $\bar{k}^\lambda$ the averaged droplet absorption or scattering coefficient at wavelength λ through pathlength $\Delta_n z$.

The averages transmission through a pathlength $\Delta_n z$ ($\bar{\tau_n}^\lambda$) is calculated as:

$$\bar{\tau_n}^\lambda = \frac{\int_\lambda \exp(-k^\lambda \Delta_n z) S_0^\lambda \,\mathrm{d}\lambda}{\int_\lambda S_0^\lambda \,\mathrm{d}\lambda},$$

where $S_{0\lambda}$ is the solar irradiance at the top of the atmosphere at wavelength λ.

The physical parametrisation has thus been displaced in the choice of the weighting factors w_n, which depend strongly on the case studied (transmissions, reflection, thin clouds, thick clouds).

Another important factor to know is the asymmetry factor, which is varying only slowly with wavelength and can thus be averaged in the following way:

$$\bar{g}^\lambda = \frac{\int_\lambda g^\lambda k_{scat}^\lambda S_0^\lambda \,\mathrm{d}\lambda}{\int_\lambda k_{scat}^\lambda S_0^\lambda \,\mathrm{d}\lambda},$$

where the subscript *scat* stands for the scattering absorption. [**31**] showed that these approximations gave very satisfactory results compared to the optical properties of water cloud types as determined by [**34**]. Ice cloud types are treated in a very similar way to water cloud ice and their optical properties can be found in [**20**]. The validity of this hypothesis has to be checked, as has been shown in chapter 2 the behavior of cirrus clouds is different from other types of clouds.

4.4.2 The impact of aerosols and greenhouse gases on radiation in CLM

The scattering and absorption done by aerosols and gases in the atmosphere can be assessed in a consistent way via the k-distribution method for large spectral bands, as proposed by [**36**]. The transmission functions for one gas or aerosol type are fitted by an exponential sum-fitting technique:

$$\bar{\tau}^\lambda(u) = \sum_{i=1}^{l} w_i e^{-k_i u},$$

where the weights w_i are constrained to sum to one, in order to ensure energy conservation. These weights are then used to affect the fluxes calculated by the resolution of (9):

$$F = \sum_{i=1}^{l} w_i F(\delta_0 + \delta_i).$$

However if more than one gas has an important absorption in a given spectral band, this calculation would require a double sum, which strongly increases computational time. To avoid this the radiative transfer is solved first without the impact of any gas, giving gray fluxes (F^0). Then we solve the problem as described above for every gas one by one, and derive an effective gaseous transmission for every layer and for every gas:

$$\bar{\tau}^\lambda = \frac{F^1}{F^0},$$

where F^1 is the flux calculated for gas one. Finally the absorption is approximated by:

$$F = \prod_{m=1}^{M} \bar{\tau}_m^\lambda F^0,$$

where the product goes over the M gases considered.

In order to take into account the pressure and temperature dependency of gaseous transmissions functions corrections are done in three steps:

- In a first step the set of w_i and k_i are computed at a given temperature and pressure.
- Next the pressure is varied in a way to obtain the least-squares fit of pressure-dependency exponents α_i:
$$\bar{\tau}^\lambda(u,p,T) = \sum_{i=1}^{l} w_i \exp\left[-k_i \left(\frac{p}{p_{ref}}\right)^{\alpha_i} u\right].$$
- Finally this step is repeated but this time for the temperature, giving exponents β_i:
$$\bar{\tau}^\lambda(u,p,T) = \sum_{i=1}^{l} w_i \exp\left[-k_i \left(\frac{T}{T_{ref}}\right)^{\beta_i} u\right].$$

After calculation these corrected transmission function will finally be given by:

$$\bar{\tau}^\lambda(u,p,T) = \sum_{i=1}^{l} w_i \exp\left[-k_i \left(\frac{p}{p_{ref}}\right)^{\alpha_i} \left(\frac{T}{T_{ref}}\right)^{\beta_i} u\right].$$

CHAPTER V

Water Vapour IN CLM

This final chapter gives the comparison of the water vapour as simulated with the regional climate model CLM, with the NCEP (National Centers for Environmental Prediction) reanalyses and AIRS satellite data. The major challenge of this comparison is the fact that the output of the regional model is at much higher resolution than the output of the global reanalysis. This fact has to be treated with particular caution.

This chapter will begin with a description of the model setup used for the runs analyzed. Next a comparison of a simulation on a $0.5° \times 0.5°$ grid for the year 2005 with the NCEP reanalysis will be done and the same simulation is compared with the *Atmopsheric Infrared Sounder* (AIRS) satellite data. Finally a comparison with the same sources is made for a simulation of January 2005 but on a model grid of $0.22° \times 0.22°$.

5.1 Model setup

As the model is non hydrostatic and as physical parametrisations are explicit, a lot of computer resources are needed to run the model. For example a simulation on the European domain (see figure 13), at a resolution of $0.16° \times 0.16°$ ($\approx$ 18km $\times$ 18km) of 24 h takes $\approx$ 16 h of CPU time, if it is run on a single processor (on one of the machines at Lemaître with a CPU at 2.6 GHz). Thus with this setup it is not practical to do climate runs (over several years). This is why the model has been designed to be run on several CPUs, which permits to cut the runtime considerably.

Due to technical reasons it was not possible to run the model on several processors for these preliminary test runs. This is why a resolution of $0.5° \times 0.5°$ ($\approx$ 56km $\times$ 56km) was chosen for these first runs, on the European domain. Every of the 20 vertical layers contains 62×70 gridpoints, giving a total of $62 \times 70 \times 20 = 89280$ gridpoints in the atmosphere where the prognostic variables of the model are calculated at every time step. In order to do fast runs and be sure of the stability of the calculations a time step of 240 s was chosen.

With this setup of the model[21] a run that was forced and initialized by NCEP reanalysis, downscaled to the CLM grid, for the year 2005 was made. The simulation of the whole year took $\approx$ 5 days. This year was chosen as the satellite data, that will be used for comparison with the output of the model, are only available from september 2003. After having a look at the temperature and precipitation for the years available, 2005 seemed to be the most "normal" year (summer not too warm compared to average temperatures and winter not too cold).

[21] It is important to note that no changes were yet made in the model code for these tests

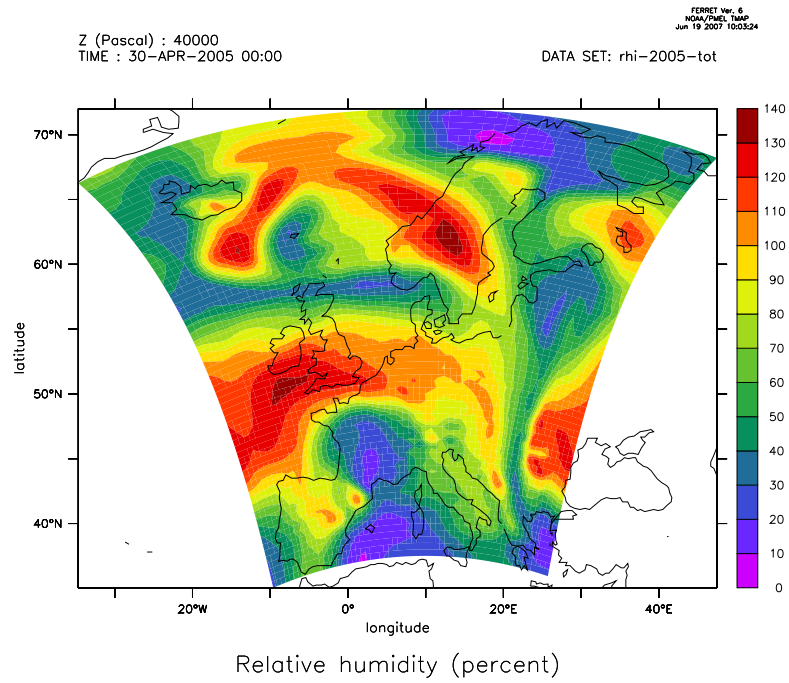

Figure 13: Relative humidity with respect to ice as modeled by CLM on the 30th April 2005 at an altitude of 400 hPa ($\approx$ 7200 m)

5.2 Evaluation of the $0.5° \times 0.5°$ setup

This section compares the temperature, the specific humidity and the cloud water content of the model with the reanalysis of the NCEP. Next a comparison with satellite data of the AIRS on the NASA Aqua spacecraft, will be done.

5.2.1 Comparison with the NCEP reanalysis

This reanalysis has been performed using the NCEP AMIP global spectral model using T62 (spacing of 209 km between grid cells) global spectral grid of 28 vertical levels. However when comparing this data, with the output of the CLM on a finer grid, caution has to be applied.

Before actually comparing the humidity of the model with the observations a general overview of the model run will be gained, by first doing a comparison for the temperature. For comparison the mean, relative error will be used[22], which is calculated in the following way:

$$MAE = \frac{1}{N \cdot M} \sum_{i=1}^{N} \sum_{j=1}^{M} |x_{reana}(i,j) - x_{CLM}(i,j)|,$$

where $x_{reana}(i,j)$ is the variable that is evaluated (in this case temperature) as given by reanalysis at point (i,j) and $x_{CLM}(i,j)$ is the corresponding value as simulated by CLM. The sums are done over all the grid-cells in the domain.

Figures 14 to 15 give the mean absolute error for the temperature at different altitudes. There are two things can that can be clearly observed on these graphs:

[22] This measure was chosen in order to compare the results to similar test made in [**3**] with the MM5 model

- The errors observed are very small, below 0.5K, and thus CLM reproduces the temperature in a coherent way to the NCEP reanalysis.
- A clear seasonal cycle is evident in the error, with MAE being lower in summer than in winter, and passing through a maximum at the beginning of spring. The temperature is thus modeled in a better way during summer than during winter time.

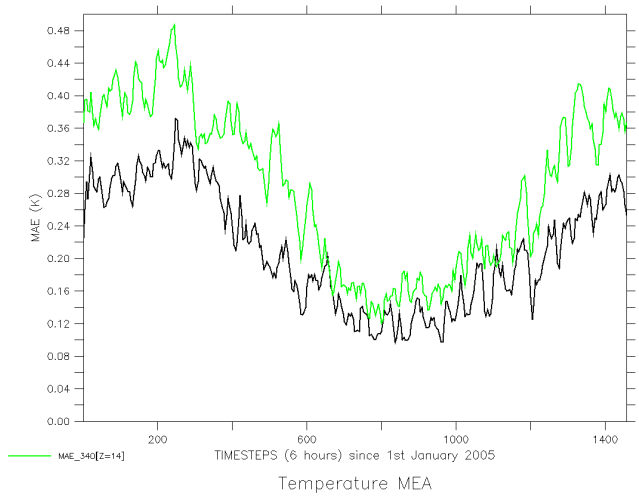

Figure 14: Mean absolute error of temperature (in kelvins) between the reanalysis and the CLM simulation at altitudes of 220 hPa (black) and 340 hPa (green) . The x-axis multiplied by 6 gives the hours since the 1st January 2005, on the European domain (see figure 13)

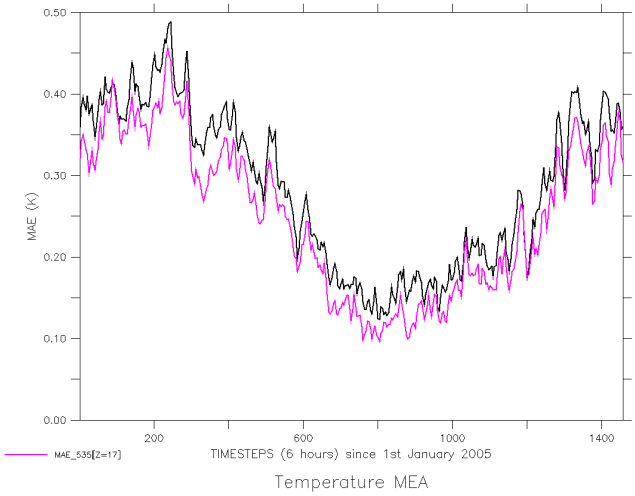

Figure 15: Same as figure 14, but at altitudes of 400 hPa (black) and 535 hPa (red)

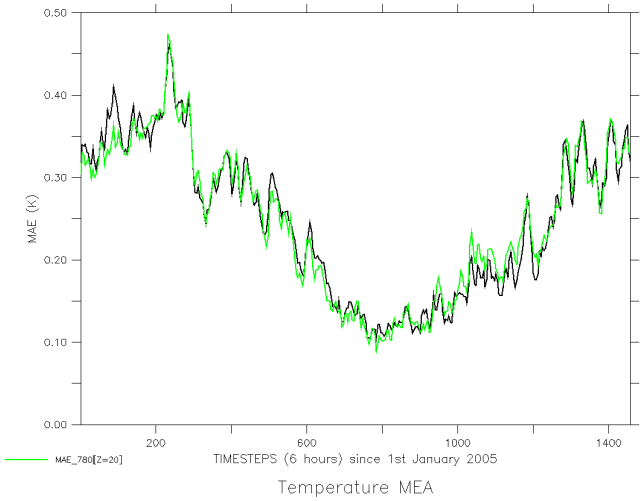

Figure 16: Same as figure 14, but at altitudes of 660 hPa (black) and 780 hPa (green)

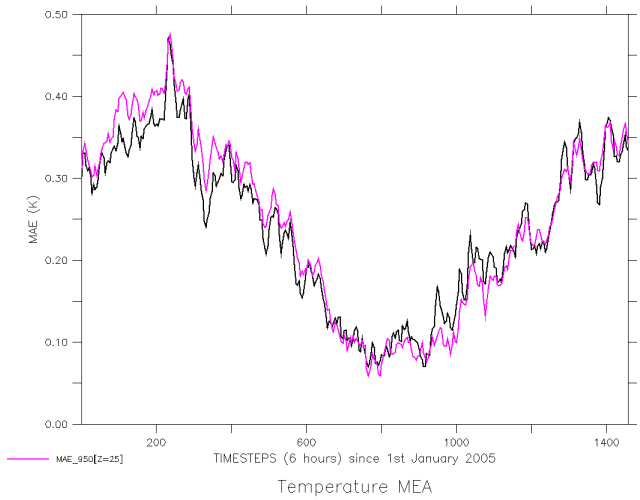

Figure 17: Same as figure 14, but at altitudes of 840 hPa (black) and 950 hPa(red)

Now we will do the same comparison between NCEP reanalysis and CLM output but this time for the specific humidity. Figures 18 to 21 give the MAE of the specific humidity[23] at different altitudes.

We can clearly observe strong divergence ($> 50\%$) at certain days between the two sources. These differences become less important as the altitude of the comparison goes down. At 600 hPa only a few days are more than 20% different, which can be considered as being a good agreement for specific humidity as was noted by [**3**]. We can also observe a small annual cycle, with a small maximum (not considering the peaks of the MAE) in summer months. On the low levels 840hPa and 950 hPa, the two have nearly the same results.

The fact that these peaks are occurring may be related to two facts:

- First as was explained in the section 4.3, subgrid cloudiness is not taken into account directly in the microphysical calculations of the model. However in the model used to do the NCEP reanalysis it is. This may explain that although the NCEP reanalysis forms clouds (and thus lowers the specific humidity) CLM does not. The cloud cover of the two models was also compared (not shown) and it was found that CLM simulated less clouds than the reanalysis, in agreement with this hypothesis.

- Alternatively it is possible that this problem is related to difference of resolution in the model. As we have seen in chapter 2, cirrus ice clouds can be vertically and horizontally in-homogeneous, and it is possible that a model at higher resolution (like CLM) can represent layers with small horizontal extension that are highly saturated but do not yet form clouds, more precisely than a model at low resolution (like the model used for the NCEP reanalysis). In order to check this hypothesis we will compare the output of CLM with the AIRS satellite data, which is at higher resolution than the reanalysis, although a case study (from in situ campaigns) will probably be necessary to conclude definitely.

[23] It was decided to give the MAE of specific humidity in percent as these figures give a better appreciation of the differences then given the MAE in $\mathrm{kg}_{water}/\mathrm{kg}_{\mathrm{air}}$.

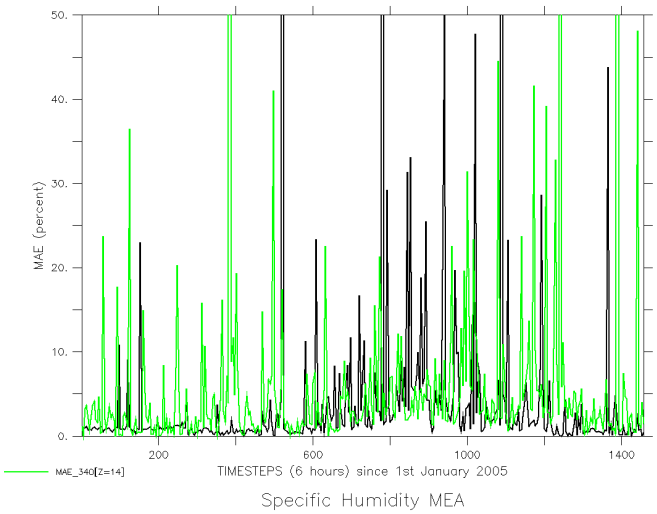

Figure 18: Mean absolute error of specific humidity (in percent) between the reanalysis and the CLM simulation at altitudes of 220 hPa (black) and 340 hPa (green) . The x-axis multiplied by 6 gives the hours since the 1st January 2005,on the European domain (see figure 13)

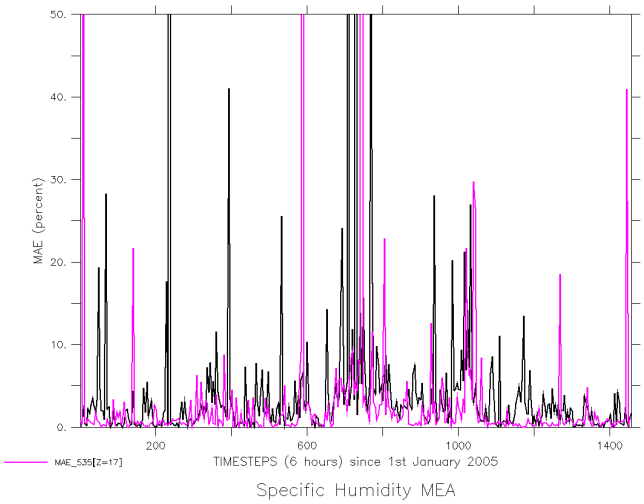

Figure 19: Same as figure 18, but at altitudes of 400 hPa(black) and 535 hPa(red)

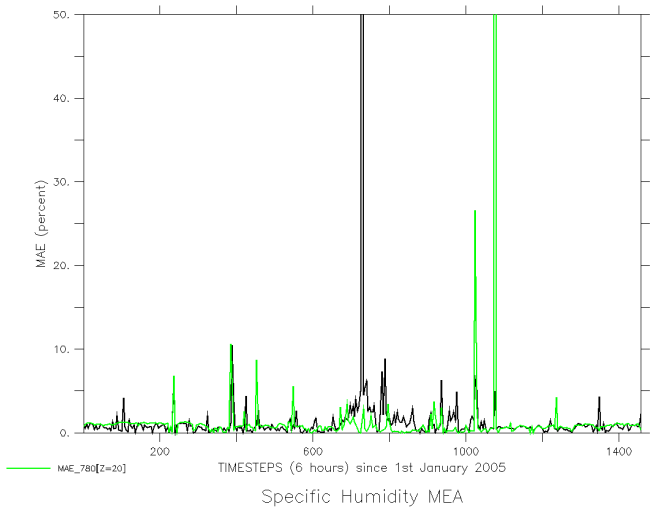

Figure 20: Same as figure 18, but at altitudes of 660 hPa(black) and 780 hPa(green)

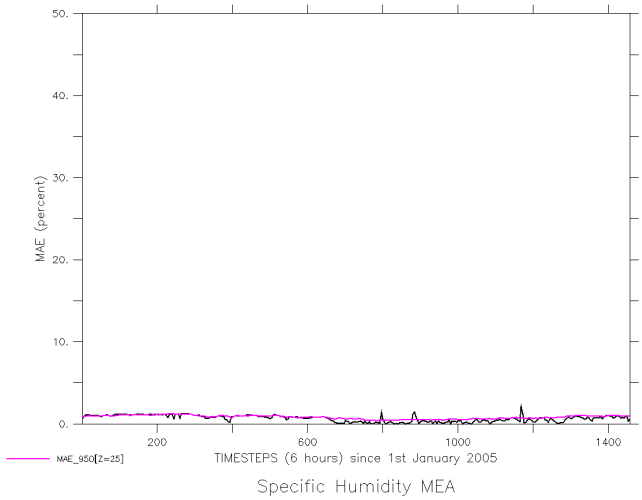

Figure 21: Same as figure 18, but at altitudes of 840 hPa(black) and 950 hPa(red)

5.2.2 Comparison with AIRS satellite data

In order to be sure that the observed problems are not due to an error in upscaling the model grid to the reanlysis, a comparison with the observation from the *Atmopsheric Infrared Sounder* (AIRS) on the NASA Aqua spacecraft will be done. This comparison also enables us to compare the output of CLM with data on a finer grid ($1° \times 1°$) than the reanalysis and data that is independent of the forcing of the model (as NCEP reanalysis are used to force the model). A description of the way these data were obtained and a validation of the data can be found in [**10**].

We will do the same analysis as in the previous section and first do a comparison of the temperature as simulated by CLM with the temperature as measured by AIRS. The results are given in figures 22 and 23.

We can clearly observe an important difference between the data and the model results (up to 20K MAE difference). Figure 24 gives the same plot as figure 23, but this time the absolute value in the definition of the MAE has not been used (thus giving the mean of the difference between CLM and the ARIS data over the region of interest). Both figures are effectively the same thus indicating that there is a clear shift between the two datasets, with the output of CLM being warmer than the AIRS data.

As the model was in good agreement for the reanalysis values, which give reliable temperature especially on ground level (due to many measuring stations), we may conclude here that this seems to indicate a problem in the comparison of the two datasets. A problem with the AIRS data is also not probable, as this data has been extensively validated by [**10**]. The difference comes probably from a different definition of the pressure levels. Whereas CLM gives the output on real pressure levels (as simulated by the model), it is possible that AIRS data are actually given on a fixed altitude (which is easier for the satellite to determine than pressure levels), and these are then transformed labeled with a pressure reference, that is obtained via a fixed relation (e.g. the standard atmosphere)[24]. The fact that the error in figure 24 always remains positive indicates that this can only be part of the problem, as we would expect the temperature to be lower or higher if the standard atmosphere was used. Other problems related to the way the data was treated can not be excluded at this stage (e.g in the way the averages were made).

Figure 25 gives the MAE between the AIRS data and CLM for the specific humidity. Only a restricted set of levels are shown here as the MEA error for the different altitudes are nearly exactly the same. We can again observe this high offset (of around 38%) of the model with the data. However it is interesting to note that if we do not consider this constant offset we can see that the scatter of the data is less important (of the order of 6%) than the very high scatter that we observed with the NCEP data. This is an indication that the resolution of model, or data we are comparing with, plays an important role when wanting to evaluate the accuracy of the specific humidity in the CLM model.

[24] Although the authors of [**10**] were asked about the definition of the pressure level it was not possible to get a clear answer

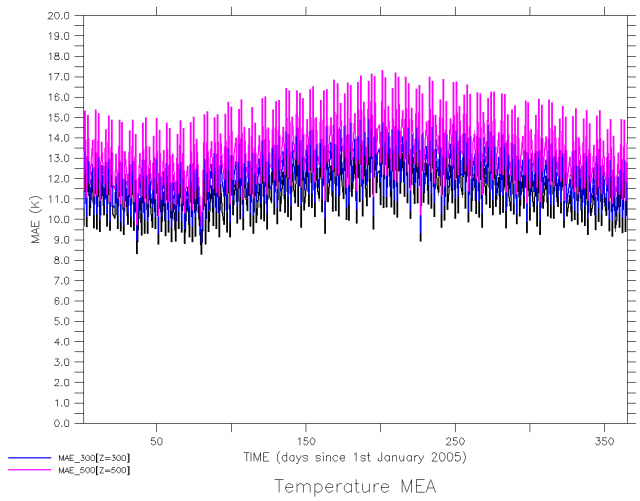

Figure 22: Mean absolute error of temperature (in K) between the AIRS satellite data and the CLM simulation at altitudes of 200 hPa(black) and 300 hPa(blue) and 500 hPa(red), on the European domain (see figure 13)

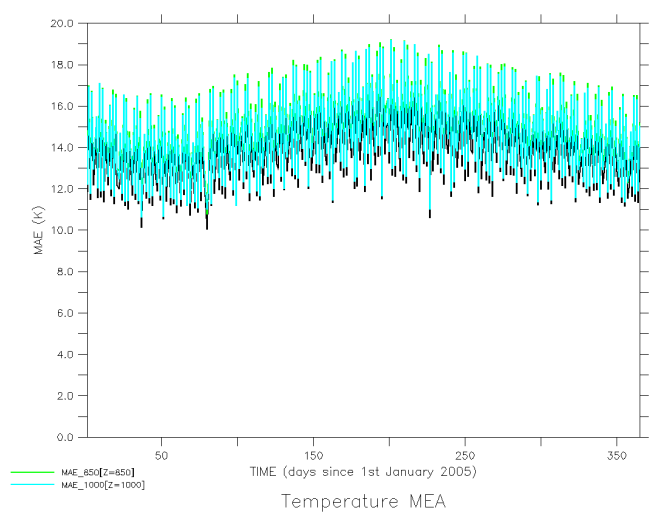

Figure 23: Same as figure22 but for altitudes of 600 hPa(black) and 850 hPa(green) and 1000 hPa(blue).

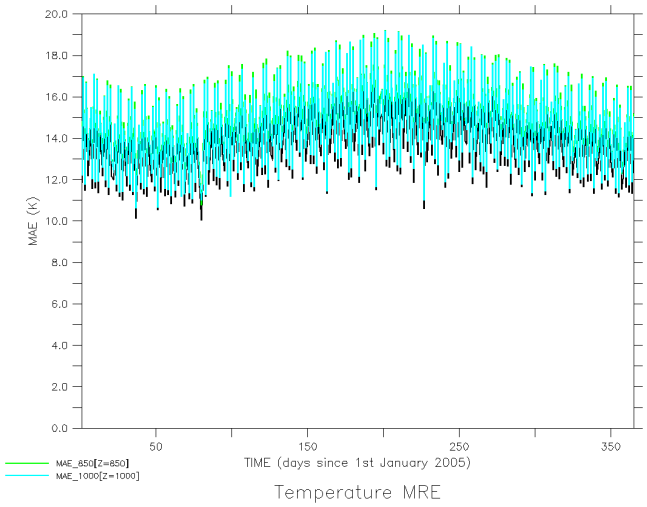

Figure 24: Mean relative error of temperature (in K) (same as MAE but without absolute error) between CLM and the AIRS satellite data at altitudes of 200 hPa(black) and 300 hPa(green) and 500 hPa(blue), on the European domain (see figure 13)

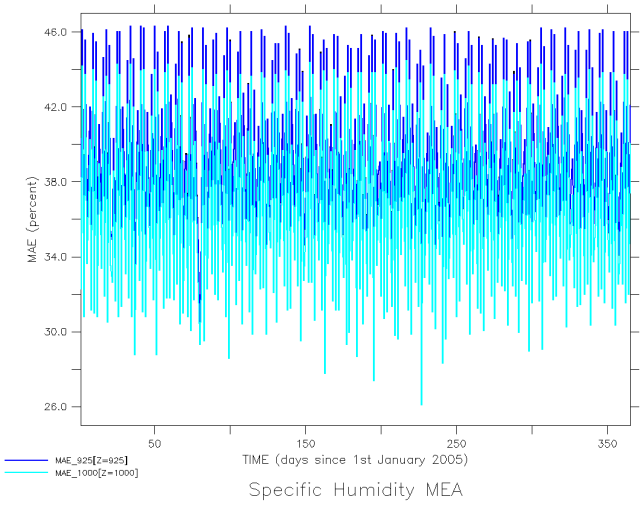

Figure 25: Mean absolute error of specific humidity (in %) between the AIRS satellite data and the CLM simulation at altitudes of 200 hPa(black) and 925 hPa(blue) and 1000 hPa(cyan), on the European domain (see figure 13)

5.3 Evaluation of the $0.22° \times 0.22°$ setup

In order to evaluate the CLM model at a different model resolution we will do the same analysis but this time the CLM model was run at a higher resolution of $0.22° \times 0.22°$ ($\approx$ 20km $\times$ 20km. Due to the fact that the it was possible to run the model only on one single processor and due to time limitations only the month of January was simulated. This will not give us a good appreciation of the climatic properties of the model, but will give us an indication of the performance of the model, especially with regard to the simulation of water vapour. Also the problem of the independency of the model to the initial conditions(that are done via the NCEP reanalysis that are downscaled to the model grid) has to be adressed. The model should be independent after 3 or 4 days (personal communication from A. Will) from the initialization and we can observe this on figure 18, as the divergences are occurring after a few days. Thus the fact to have such a short time period seems acceptable for a first impression. In this section we will do again first a comparision with the NCEP data is performed and next with the AIRS satellite data.

5.3.1 Comparison with the NCEP reanalysis

As in the previous section the mean absolute error will be used to compare first the temperature and next the specific humidity over the simulation period.

Figures 26 and 27 give the mean absolute error at different altitudes between the temperatures of the temperature as simulated by CLM and the NCEP reanalysis[25] . Again we can see a close correlation between the temperature as simulated by the regional model and the reanalysis. The order of magnitude of the MAE is the same as for the model setup at $.5° \times .5°$.

Figures 28 and 29 give the MAE of the specific humidity compared between CLM and the NCEP reanalysis. We can again observe these 'spikes' which indicate large errors ($> 50\%$) on certain days and n acceptable agreement between these days (MEA $< 15\%$). This indicates that running the model at higher resolution does not bring any substantial improvements as concern this comparison which sustains the hypothesis that the problem is related to NCEP grid resolution not the CLM resolution, given in section 5.2.1.

[25]It is interesting to note that the output of CLM and the NCEP reanalysis do not agree on the first day. The reanalysis was in fact used to initialize the model, however it had to be downscaled to the model grid to do so, which explains the differences observed.

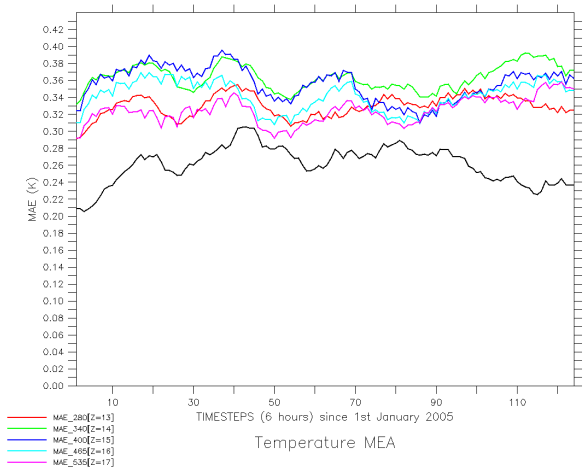

Figure 26: Mean absolute error between temperature as simulated with CLM and the NCEP reanalysis. The different colors correspond to different altitudes, 535 hPa(pink), 465 hPa(cyan), 400 hPa(blue), 340 hPa(green), 280 hPa(red) and 220 hPa (black). The horizontal axis gives the number of output time-steps (6 hours) since the 1st January 2005, on the European domain (see figure 13)

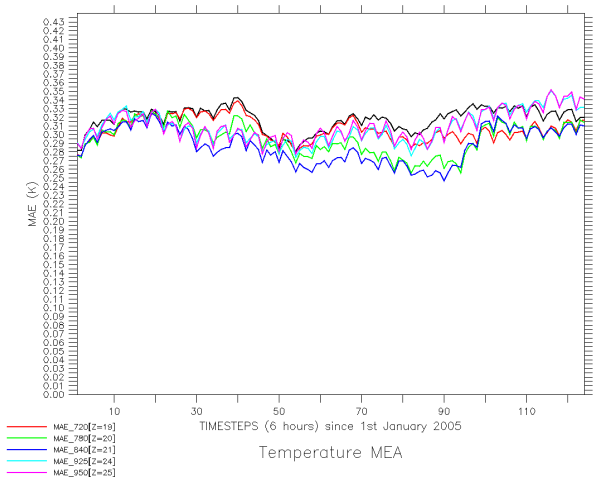

Figure 27: Same as figure 26 but altitude, 650 hPa (black), 720 hPa (red), 780 hPa (green), 840 hPa (blue), 925 hPa (cyan) and 950 hPa (pink).

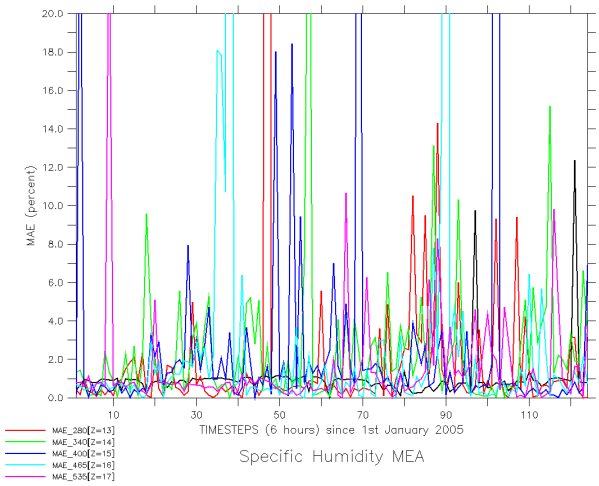

Figure 28: Mean absolute error between specific humidity (in percent) as simulated with CLM and the NCEP reanalysis. The different colors correspond to different altitudes, at 535 hPa(pink), 465 hPa(cyan), 400 hPa(blue), 340 hPa(green), 280 hPa(red) and 220 hPa (black). The horizontal axis gives the number of output time-steps (6 hours) since the 1st January 2005, on the European domain (see figure 13)

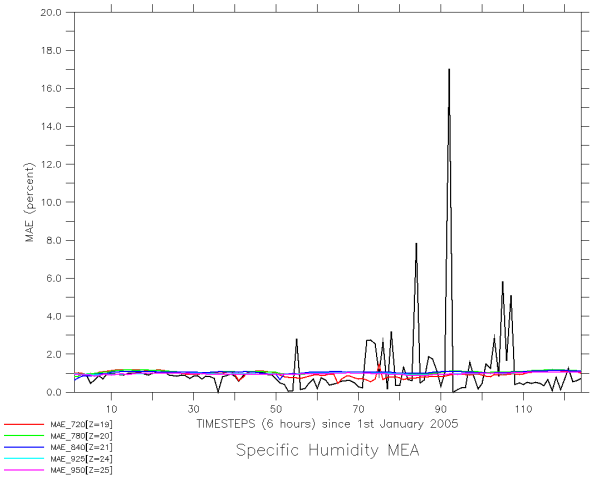

Figure 29: Same as 28 but altitude at 650 hPa (black), 720 hPa (red), 780 hPa (green), 840 hPa (blue), 925 hPa (cyan) and 950 hPa (pink).

5.3.2 Comparison with AIRS data

In this last section we will perform a comparison of the output of the CLM model on a $0.22° \times 0.22°$ grid with the AIRS satellite data. Figure 30 and 31 give the temperature comparison. Plotting the same curve but ignoring the absolute value in the definition of the MAE, we observe the same curve as previously (not shown). From this we can conclude that at this higher resolution we can again observe the high offset of the curves, of the same order of magnitude as previously and which is probably at least partially due to a different definition in pressure layer.

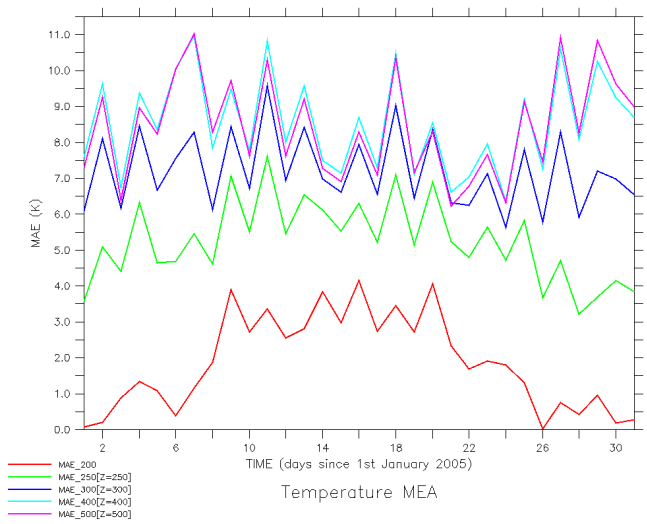

Figure 30: Mean absolute error of temperature (in K) between the AIRS satellite data and the CLM simulation. The different colors correspond to different altitudes, at 200 hPa (red), 250 hPa (green), 300 hPa (blue), 400 hPa (cyan) and 500 hPa (pink), on the European domain (see figure 13)

Next we are going to compare also the humidity of the model to the satellite, data, which gives us figure 32. Again little variation is observed between the different altitudes, so only a few of them are plotted. The order of magnitude of the error is again the same as at lower resolution and the range of the noise is also on the same order of magnitude, thus indicating that in the comparison with satellite data, the grid on which the model is run does not play an important role as long as the problem with strong difference between the two data-sets is not resolved.

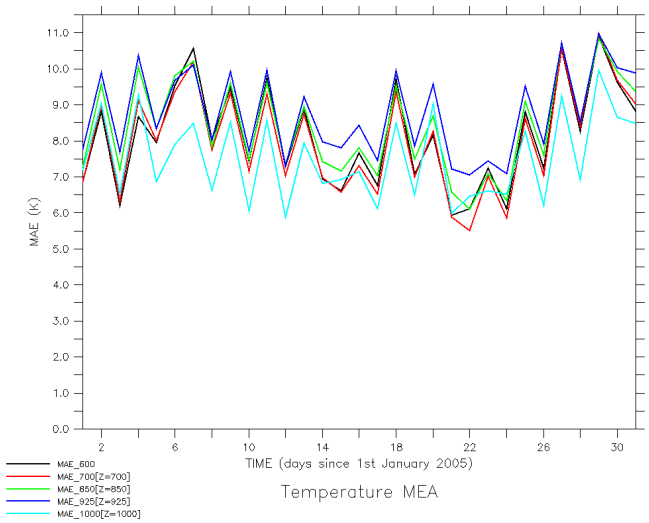

Figure 31: Same as figure 30 but altitudes at 600 hPa (black), 700 hPa (red), 850 hPa (green), 925 hPa (blue) and 1000 hPa (cyan).

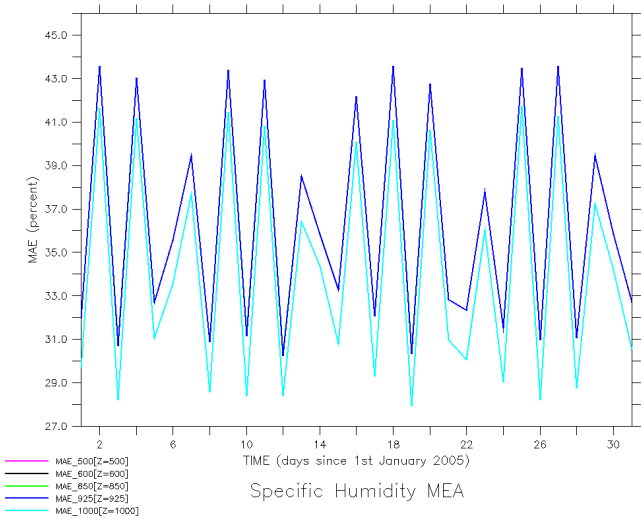

Figure 32: Mean absolute error of the specific humidity (in %) between the AIRS satellite data and the CLM simulation. The different colors correspond to different altitudes of 200 hPa(black) and 300 hPa(blue) and 500 hPa(cyan).

Conclusion and Outlook

This first thesis year has given us an insight into the microphysics of clouds and in particular cirrus clouds, the problems related to measuring or modelling the microphysical and radiative problems of cirrus clouds, and a first insight into the use of a regional climate model, the parametrisation of ice cloud microphyics in such a model and the validation of it.

This report first gave an introduction to the problem of climate impacts of aviation, the general subject of the underlying PhD thesis and motivation for this work as well as the use of regional climate model for this task. Preliminary results from the ABCI project were presented showing that the local regional forcing in central Europe, especially in Belgium due to contrails and AIC is of the same order of magnitude as total anthropogenic forcing of CO_2.

We then continued by giving a general overview of the microphyiscial and radiative properties of cirrus clouds in the mid latitudes and in particular over Europe. This chapter showed that a number of in situ measurements campaigns that have been performed, which showed radiative properties, that are of crucial importance for climatic studies depend strongly on the type of particles that form the clouds as well as their density. These studies also showed that the optical properties of cirrus clouds, that are very important for a correct simulation of cirrus clouds in climate models, are still poorly known

Chapter 3 gave a theoretical description of the different processes that are involved in forming ice particles in cloud, and the interactions between them. This analysis showed that it is often possible to get an accurate description of the different phenomena, but these can not always be translated into a parametrisation to be used in a climate model, as it would be to expensive in computer time.

Next we showed how the different processes described in the previous chapter were implemented in the CLM regional climate model, that was chosen to be used for this thesis. In particular we pointed out the main weaknesses of the different parametrisations, including the fact that the micro physical model of CLM needs the whole grid cell to be supersaturated with respect to water in order to form clouds, and the subgrid cloudiness is determined in a different part of the model, which is then used to calculate the radiation influenced by clouds and perform a correction of the microphysical properties calculated.

The final chapter of this report then gave an analysis of the first runs made with CLM, giving an special attention to the water vapour, as this was determined to be of crucial importance for the determination of the impact of contrails and AIC on climate. Two runs were analyzed: The first run was on a $0.5° \times 0.5°$ grid and the simulation was made over the whole year of 2005. The second run was on a $0.22° \times 0.22°$ grid, but only a simulation of January of 2005 could be performed.

For both simulations there was a good agreement found for temperature between the regional model output and the NCEP reanalysis, which indicated that the temperature was simulated in a correct way by the model, and on the ground and at high altitudes.

For the same comparison of the model with the AIRS satellite data an large temperature offset was found (the CLM model simulates higher temperatures than the satellite observations). As the model run reproduced the reanalysis in a proper way and as the satellite data has also been validated it was suggested that this could at least partly be due to a different definition of the pressure levels in the satellite data and the regional model. An error in the post-processing of the data cannot be excluded. This will be checked by performing a run of the regional model

and interpolating the output to altitudes levels which correspond to the levels of the AIRS data.

For the comparison of the specific humidity as it was simulated by the regional model with the NCEP data, we observed for both simulation runs important errors on certain days, whereas between these days the agreement was quite good. This could be related on the one hand to the fact that the subgrid scale cloudiness is not correctly simulated by CLM, or to a problem of comparing models on a wide grid with the reanalysis, which are done on a wider grid. This last hypothesis seems to be verified, due to the fact that both model runs, on different grids show divergences with respect to the reanalysis that are on the same order of magnitude (the microphysical parametrisation of CLM should reproduce the cloudiness in a better way on a finer grid, if there was no correction for sub-gid scale cloudiness made) and the comparison with the AIRS data (which is on a finer grid than the reanalysis) shows that the agreement is better, although we can observe again an important offset.

In order to verify these hypotheses and to validate the quality of the model in the upper troposphere we will first try to resolve the problem of the levels between the regional model and the AIRS data, and use this data to do a general validation of the model. In situ measurements, like samples retrieved by commercial aircrafts (which are done in the MOZAIC[26] project) can then be used to do a case by case validation of the regional model at higher resolution.

5.4 Next steps

The next step in the process of the PhD thesis will then be to introduce a parametrisation of contrails into the model. It is planned to use two different parametrisations, a first rather simple one proposed by Ponater et al. [**27**] and next a more detailed one which is currently developed at CERFACS in Toulouse based on Large Eddy Simulation (LES) simulation of the plume behind flying aircrafts, but which is still being developed.

The Ponater parametrisation is based on the fact that more clouds are formed where planes are producing contrails. The idea is to reduce the critical humidity above which clouds are formed that is estimated by the model. This reduction is only done where the Appleman-Schmidt criterion is satisfied and it is function of the number of planes flying in the grid-cell.

Once this parametrisation is adapted to the model, first test runs will be made and the cloudiness will be compared to contrails cover observed by satellites. Later one when the parametrisation of CERFACS is implemented it can be compared to the simpler version of the parametrisation.

[26] for more information have a look at http://www.cnrm.meteo.fr/dbfastex/datasets/moz.html

ANNEX A
Physics of ICE CRYSTALS

This annex will give examples of how the different processes related to formation and melting of snow ice can be mathematically parametrised. This gives a supplementary information to chapter 3. However the parametrisation presented here are only a choice of many different ways published. They have been chosen because they can be derived directly from observations, but are often too expensive in calculation time to be put into an atmospheric model. The following sections are based on [**28**]

A.1 Accretion processes

In this section we will similarly to section 3.2.6 consider two types of particles, denoted by X and Y. The accretion process consists of a variation in time of the mixing ratio of one of the two types of particles, by collision and coalescence with the other type of particles.

We will now suppose that particle of type X are collecting particles of type Y located on their trajectory. Lets consider a single particle X and calculate the number of particles Y, that have a reparation $n_{D_y}\mathrm{d}D_y$, that are collected by this particle X during a time $\mathrm{d}t$.

To calculate this number we need to know the product of the volume which is traversed during this time :

$$V = \frac{\pi}{4}(D_x + D_y)^2|U_{D_x} - U_{D_y}|\mathrm{d}t,$$

where D_x and D_y is respectively the diameter of X and Y particles and U_{D_x} and U_{D_x} their fall velocity. This volume then needs to be multiplied by the number of particles per unit volume, given by: $n_{D_y}\mathrm{d}D_y$ as well as the coefficient of collision designated by E (= the product of collision and coalescence efficiencies) (see section 3.2.6).

This yields that the number of particles collected by X during its fall during time interval $\mathrm{d}t$ is given by:

$$n_x = \frac{\pi}{4}(D_x + D_y)^2|U_{D_x} - U_{D_y}|\mathrm{d}t\, n_{D_y}\mathrm{d}D_y E.$$

As we are interested in a result as function of mixing ratio, we are going to express this last relation in terms of masses. To achieve this we are going to multiply this expression by the mass of the particle Y, corresponding to the diameter D_y and a falling speed of U_{D_y} $(m(D_y))$. This then gives the mass of particles Y that are collected by particle X.

As we know that there are $n_{D_x}\mathrm{d}D_x$ particles of diameter D_x and having a fall velocity U_{D_x} par unit volume, every one of this particle will contribute to the same amount to the accreation of particle Y by particles X, thus giving:

$$\mathrm{dq_x} = \frac{\pi}{4}(\mathrm{D_x} + \mathrm{D_y})^2|\mathrm{U_{D_x}} - \mathrm{U_{D_y}}|\mathrm{dt\,n_{D_x}dD_x\,n_{D_y}dD_y\,m(D_y)\,E}.$$

Up to now we only considered particles that are in the range of sizes between D_i and $D_i + \mathrm{d}D_i$ where $i \in \{X, Y\}$. As particles have are dispersed over a large spectrum of diameters and fall velocities, we thus need to integrate over the whole spectrum:

$$\frac{\partial q_x}{\partial t} = \frac{\pi E}{4\rho}\int_0^\infty n_{D_x}\left(\int_0^\infty (D_x + D_y)^2|U_{D_x} - U_{D_y}|\mathrm{d}t\, n_{D_y} m(D_y)\mathrm{d}D_y\right)\mathrm{d}D_x. \tag{10}$$

We are now going to use this formula to determine the accretion factor between different particles present in the accretion processes related to ice particles. For those particles being in suspension in the air, we can suppose that the fall velocity is zero an thus the formula simplifies.

A.1.1 Accretion of ice crystals by rain

To calculate this conversion term we use equation (10) in which we consider the X particles to be rain drops and the Y particles to be ice crystals.

The rain drops are considered to have a Marshall-Palmer log-normal distribution and thus their concentration if given by: $n_{D_r} = n_{0_r}\exp(-\lambda_r D_r)$ where n_{0_r} is an empirical parameter, determined by Marshall-Palmer to be $n_{0_r} = 8 \cdot 10^{-2}\mathrm{cm}^{-4}$ and λ_r is the dispersion parameter of rain drops. The fall velocity of rain drops is given by: $U_r = a_r D_r^b(\rho_0/\rho)^{1/2}$, following a parametrisation by [**21**]. The constant a and b have been determined to fit data best if they are taken as: $a_r = 842\,\mathrm{m}^{0.2}/\mathrm{s}$ and $b = 0.8$.

As the ice crystals are suspended in the air the fall velocity is taken to be zero[27], and they have a mass per unit of volume of m_{D_i}.

Introducing all this into equation (10), we get:

$$\frac{\partial q_r}{\partial t} = \frac{\pi E}{4\rho}\underbrace{\int_0^\infty n_{0_r} a_r \exp(-\lambda_r D_r) D_r^{b+2}\mathrm{d}D_r}_{1}\underbrace{\int_0^\infty \frac{n_{D_i} m_{D_i}}{\rho}\mathrm{d}D_i}_{2}. \tag{11}$$

By definition of the gamma function, the first integral of equation (11) yields $\Gamma(b+3)/\lambda_r^{b+3}$. For the second part we have to remark that the mixing ratio of ice particles is given by: $\rho q_i = \int_0^\infty n_{D_i} m_{D_i}\mathrm{d}D_i$. Substituting into (11) we get:

$$\frac{\partial q_r}{\partial t} = \frac{\pi E}{4} q_i n_{0_r} a_r \left(\frac{\rho_0}{\rho}\right)^{1/2}\left(\frac{\Gamma(b+3)}{\lambda_r^{b+3}}\right).$$

A.2 Homogenous nucleation

The number of ice crystals that are formed in a unit of volume during a second, can be determined from a molecular view as:

$$J = \frac{kt}{h}\exp(-(\Delta G' + \Delta G t)/kt),$$

[27] This is only as rough approximation for cirrus cloud as has been showed in section 2.6

where k is the Stefan-Boltzmann constant and h the Planck constant. ΔG is the energy needed to increase the free energy of the surface if this surface is increased. This term can be described as a function of density, temperature, the latent heat and the surface tension, which is defined to be the work per unit of surface that is needed to increase the free energy of the surface.

On the other hand $\Delta G'$ designates the energy needed to diffuse molecules of water through the interface surface of water and ice. It is quite difficult to find an appropriate parametrisation other than by experimental way. As we have discussed in section 3.2.1 experimental evidence has shown that homogeneous nucleation only occurs at temperatures below $-40°$C, and we will adapt here a simplified parametrisation saying that if the temperature drops below this threshold there is immediate freezing:

$$q_i = q_i + q_w \quad q_w = 0 \quad \text{if } T < -40°\text{C}.$$

The part of this process that results from water vapour diffusion does not contribute to increase the number of ice particles, but increases their size. Modeling this second contribution is identical to modeling the heterogeneous nucleation that we are going to develop in section A.3, with the difference that for heterogeneous nucleation the temperature range between 0°C and $-40°$C and there is a prescribed concentration of active nuclei.

A.3 Heterogeneous nucleation from water vapour

This section does only include a part of the heterogeneous nucleation of ice particles. The other processes necessitating a contact including the contact of a drop and nucleation nucleus, as well as the freezing of drops by immersion are not described.

As mentioned at the end of section A.2 the process of heterogeneous nucleation is only active at temperatures between 0°C and $-40°$C and we will prescribe a distribution of active freezing nuclei n_s, following [**8**][28]:

$$n_s(T) = n_0 \exp(\beta(273.19 - T)),$$

where β varies between 0.4K^{-1} and 0.8K^{-1} and $n_0 = 10^{-2}\text{m}^{-3}$.

Supposing that the ice particles produced have a mean mass of 10^{-12}kg, we can define a first ratio as:

$$P_{hete} = \frac{10^{-12} n_s}{\rho \Delta t} \quad \text{if } \rho q_i < 10^{-12}.$$

We are now going to calculate the contribution of water vapour (P_{vap}) and the final ratio will be the minimum of P_{hete} and P_{vap}.

Consider a parcel of air, at temperature T and of specific humidity q. If supersaturation with respect to ice is appearing, we will suppose that there is a deposition on the freezing nuclei. This deposition heats the air and its temperature is passing from T to $T + \Delta T$. If the specific water vapour at saturation is designed by q_{si}, its value at the considered temperature is $q_{si}(T + \Delta T)$. Thus the heating of the air is given by:

$$\Delta T = \frac{L_s}{c_p}[q - q_{si}(T + \Delta T)], \tag{12}$$

where L_s is the latent heat of vapourization of water and c_p is the specific heat of the air.

[28] This formula is in accordance with the properties we mentioned in section 3.2.3: in contrast to condensation nuclei, freezing nuclei, which are insoluble, present an activity that depends on temperature.

The second term in square brackets of this equation can be rewritten following the Clausius-Claperyon equation:

$$q_{si}(T+\Delta T) = q_{si}(T) + \frac{\partial q_{si}}{\partial T} = q_{si}(T)\left[1 + \frac{L_a \Delta T}{R_v T}\right],$$

where R_v is the gas constant for water vapour. Isolating ΔT in this equation and substituting into equation (12), we get:

$$P_{vap} = \frac{q - q_{si}(T)}{\mathrm{d}t}\left[1 + \frac{L_s q_{si}(T)}{c_p R_v T^2}\right]^{-1}.$$

And finally as we mentioned already the actual ratio of heterogeneous nucleation is given by:

$$S_{final} = \min(P_{vap}, P_{hete}).$$

A.4 Bergeron process

As explained in section 3.2.4, the Bergeron process, leads to a growing of ice crystals, while the droplets are disappearing. The increase in mass can be parametrized following [**18**]:

$$\frac{\mathrm{dm}}{\mathrm{dt}} = a_1 m^{a_2},$$

with a_1 and a_2 parameters that have been determined by Koeing in order to fit observational data. Using the fact that $S_{berg} = 1/\rho(n_s \frac{\mathrm{dm}}{\mathrm{dt}})$, as well as the definition of the mixing ration: $\rho q_i = n_s m$, we finally get:

$$S_{berg} = \frac{1}{\rho}\left[n_s a_1 \left(\frac{\rho q_i}{n_s}\right)^{a_2}\right].$$

A.5 Sublimation of ice crystals

In this section we will establish how ice crystals grow as a function of the degree of supersaturation and ambient temperature. If there is no accretion the ice crystal is in equilibrium with the environment an we can write, following the definition of the latent heat:

$$4\pi k_h R(t_D - t_A) = 4\pi R L_s D_{wa} \Delta\rho_v,$$

where L_s is the latent heat of sublimation, k the thermal conductivity, R the dimension of ice crystals and D_{wa} the diffusivity of water vapour in the air.

The perfect gas equation writes for water vapour: $q_l = \rho_v R_v T_a$, with T_a the ambient temperature and for the ice crystal: $q^v_{sw} = \rho_i(R) R_v T_i$, where q^v_{sw} is the saturation pressure with respect to water vapour, $\rho_i(R)$ is the density of the ice crystal at radius R and T_i is the temperature of the crystal. These two relations can then be integrated into the previous relation to yield:

$$\frac{q_l - q^v_{sw}}{T_a(T_i - T_a)} = \frac{R_v k_h}{D_{wa} L_s} \tag{13}$$

If we suppose that the ice crystal is growing with spherical symmetry,the mass accretion with respect to time can be written as:

$$\frac{\mathrm{dM}}{\mathrm{dt}} = 4\pi R D_{wa}(\rho_v - \rho_i(R)) = \rho_i \frac{\mathrm{dV}}{\mathrm{dt}} = \rho_i 4\pi R^2 \frac{\mathrm{dR}}{\mathrm{dt}},$$

Taking the second and the last of these relations we may write:

$$R\frac{\mathrm{dR}}{\mathrm{dt}} = (D_{wa}/\rho_i) \cdot (\rho_v - \rho_i(R)).$$

Substituting the perfect gas relation we get:

$$R\frac{\mathrm{dR}}{\mathrm{dt}} = \frac{D_{wa}}{\rho_i R_v T_a}(q_l - q^v_{sw}).$$

Isolating the difference $q_l - q^v_{sw}$ from equation (13) and substituting in this last equation we finally get:

$$R\frac{\mathrm{dR}}{\mathrm{dt}} = \frac{k}{\rho_i L_s}(T_i - T_a). \tag{14}$$

Dividing equation (13) by the saturation pressure at ambient temperature ($q^v_{sw}(T_a)$), we get:

$$\frac{q^v_{sw}}{q^v_{sw}(T_a)} = \frac{q^v_{sw}(T_i)}{q^v_{sw}(T_a)} + \frac{\rho_g R_v T_a}{q^v_{sw}(T_a) D_{wa}} R\frac{\mathrm{dR}}{\mathrm{dt}}. \tag{15}$$

Integration the Clausius-Clapeyron relation:

$$\frac{\mathrm{dq^v_{sw}}}{q^v_{sw}} = \frac{L_s}{R_v T^2}\mathrm{dT},$$

from $q^v_{sw}(T_a)$ to $q^v_{sw}(T_i)$, we get:

$$\ln \frac{q^v_{sw}(T_i)}{q^v_{sw}(T_a)} = \frac{L_s}{R_v T_a T_i}(T_i - T_a).$$

As we are close to equilibrium, the ambient temperature(T_a) and the temperature of the ice crystal (T_i) are nearly identical, so we may write $T_a T_i \approx T_a^2$, giving us the relation:

$$\ln \frac{q^v_{sw}(T_i)}{q^v_{sw}(T_a)} = \frac{L_s}{R_v T_a^2}(T_i - T_a).$$

Isolating $(T_i - T_a)$ in this equation and introducing into equation (14), we obtain:

$$\frac{q^v_{sw}(T_i)}{q^v_{sw}(T_a)} = \exp\left(\frac{L_s^2 \rho_i}{k R_v T_a^2} R\frac{\mathrm{dR}}{\mathrm{dt}}\right).$$

Introducing this relation into (15) we finally get the growth of the ice crystal as a function of supersaturation with respect to ice ($S_i = q_l/q^v_{sw}(T_a)$):

$$S_i = \exp\left(\frac{L_s^2 \rho_i}{k R_v T_a^2} R\frac{\mathrm{dR}}{\mathrm{dt}}\right) + \frac{\rho_g R_v T_a}{q^v_{sw}(T_a) D_{wa}} R\frac{\mathrm{dR}}{\mathrm{dt}}.$$

In order to solve this equation we see that it is of the form: $S_i = e^{ax} + bx$, with $x = \mathrm{dR}/\mathrm{dt}$. Remarking that $ax \ll 1$ we can develop the exponential as a Taylor series: $S_i = 1 + ax + bx$ thus giving us the solution: $x = (S_i - 1)/(a + b)$. This then gives us the mass growth rate with respect to supersaturation:

$$\frac{\mathrm{dM}}{\mathrm{dt}} = \rho_g 4\pi R \frac{S_i - 1}{a + b}, \tag{16}$$

with $a = (L_s^2 \rho_i)/(k_h R_v T_a^2)$ and $b = (\rho_g R_v T_a)/q_{sw}^v(T_a) D_{wa})$.

This then yields directly to the formulation of the process of sublimation of ice crystals, given by:

$$S_{icesub} = 1/\rho_i n_s \bar{f}_i \frac{\mathrm{dM}}{\mathrm{dt}},$$

with $\bar{f}_i$ a parameter to take into account the ventilation, that was determined experimentally by [**8**].

ANNEX B

Calculations of aviation radiative forcing

This annex will describe in detail how the bar chart (figure 3) has been obtained and what crucial hypotheses had to be taken to process it. Here are the figures underlying the calculations as well as the results.

Region	Flight Distance (million nautical miles)	Percentage of region movements	Fuel use >FL240 (kt)	Fuel use <FL240 (kt)	NO_x emitted (kt)
Belgium overflights	103	70.5	225	184	12
Belgium LTO	44	29.5	8	163	5
Belgium total	147	100.0	234	346	17
Europe overflights	21	0.7	152	≈0	2
Europe LTO	2 912	99.3	12 278	9 272	285
Europe total	2 935	100.0	12 427	9 272	287
World	17 720	100.0	91 736	62 232	2 033

Table 2: Flight movements and emissions as determined for the different regions considered

Table 2 gives an estimation of the traffic in 2002 in the different considered areas (Belgium and Europe) as well as for aircraft taking off and landing (LTO) in these areas and those overflying it. Please note that these figures are only first estimations and are based on a number of assumptions that are detailed hereafter and are to be improved eventually in the second half of this year.

Table 3 gives the radiative forcing (RF) of total anthropogenic CO_2, CO_2 emitted by aircraft, the RF of ozone produced by air traffic, contrails and aircraft induced cloudiness (AIC). Where applicable a distinction was made between the different regions considered.

Region	RF CO_2 all anthropogenic sources (mWm^{-2})	RF CO_2 aviation (mWm^{-2})	RF O_3 aviation (mWm^{-2})	RF contrails (mWm^{-2})	RF aircraft induced cloudiness (mWm^{-2})
Belgium	1600 (1490-1830)	25 (17.5-32.5)	70 (45-100)	350 (200-520)	1000 (340-2700)
Belgium overflights				340 (195-500)	970 (330-2600)
Belgium LTO				10 (5-20)	30 (10-100)
Europe				150 (80-210)	430 (140-1150)
Europe overflights				3 (1-5)	425 (138-1135)
Europe LTO				147 (79-205)	425 (138-1135)
World			22 (14-32)	10 (6-15)	30 (10-80)

Table 3: Radiative forcings from different agents averaged on different regions

The rest of this annex will give details about the calculations and hypotheses made to obtain the figures in these two tables.

The fuel used by aircraft that takeoff and/or land (LTO) in Belgium is small compared to the global fuel used by aviation (less than 1%) but on the other side Belgium is situated in one of the regions of the world where the air traffic is most important, due to the fact that the country is surrounded by 4 major HUB-airports of the world (London, Amsterdam, Frankfurt and Paris). Thus it seems clear that the impact of contrails and cirrus clouds as well as that due to ozone from aircraft overflying the Belgian territory (66% of all the flight movements in the Belgian airspace are overflights) is much more important than from the aircraft that actually land and/or take off in Belgium and contribute to its economic development.

One of the aims of the ABCI project is to give a precise idea of this imbalance. At the present state of the project it is not yet possible to give precise figures, due to the fact that the processing of the database of flight movements over Belgium is not yet complete (no indication of NO_xemitted and no precise indication of fuel use for historic emissions) and the regional climate model that will be used to evaluate the impact of aircraft in Europe and in particular of Belgium, is not yet operational.

This section will try however to give a first estimation of the impacts of contrails, AIC and ozone due to overflights compared to the same impacts for flights taking off and landing in Belgium and compare this situation to the situation in Europe, where overflights without landing or take-off in Europe represent less than 1% of total flight movements. At a later state of the project this table will be updated with more precise figures.

B.1 Calculations of emissions

In a first step the ratio of flight movements LTO in the region considered and those that overfly it is calculated. For Europe figures published in the Eurocontrol were used [**4**], and for Belgium the figures from [**24**] were used.

These ratios were then used to interpolate the figures published in the AERO2k database made by Manchester University for the LTO aircraft and the overflights for distance flown and NO_x emitted (it was not yet possible to distinguish the emissions of NO_x at different altitudes, which would be necessary for an exact evaluation as the impact of ozone is changing with altitude, as shown by [**7**] and [**14**]).

As shown by [**32**], the contrail coverage and thus the impact of these contrails is directly proportional to local fuel use. For this study a distinction was made between fuel used below and above FL240 (24,000ft ≈ 8000m). In fact below this altitude the atmosphere is too warm for contrails to form [**3**]. As the AERO2k database gives the fuel use for every flight level, fuel use below and above FL240 for every region could be directly deduced. However this database does not give an indication about the distinction between aircraft performing a part of their LTO cycle in the region and the aircraft overflying it.

In order to do so the following assumptions were made:

- Aircraft overflying Europe are supposed to fly all above FL240.
- Most of the passenger aircraft taking off or landing in Belgium will stay below FL240. However Business jets are capable of climbing much faster than regular passenger jets and thus will be able to reach FL240 before leaving the Belgian territory. Thus it was supposed that aircraft performing a part of their LTO cycle in Belgium only reach FL240 if they are Business jets. Figures from [**5**] indicate that ≈10% of flight movements are performed by business jets. To take into account that these jets have to climb up to FL240 only 5% of the fuel used over FL240 was attributed to aircraft performing part of their LTO cycle in Belgium.

As a general rule, it is often difficult to compare data originating from different sources. This is obviously also the case when comparing AERO2k data with data provided by [**24**]. Hereunder, we provide some indications on factors which might explain these differences:

- The assessed years are different for both publications, which explains part of the difference between both publications.
- The representative aircraft used in [**24**] correspond to the type aircraft of EMEP/Corinair which differ slightly from the type aircraft used in AERO2k. Also the calculation of the fuel use in AERO2k is more complex than the calculation of the fuel use in [**24**].
- The database used in AERO2k is a general database based on the commercial Back Aviation database, while the database used by [**24**] is a database containing all of the movements as provided directly by the Belgian air traffic management services. The data used by [**24**] are consequently likely to be more extensive for the specific Belgian territory.
- The database of AERO2k is an European database, so the specific data for Belgium might present a lower resolution (one degree by one degree) as compared to the specific Belgian data (exhaustive list of flights in the Belgian airspace) used in [**24**].
- The AERO2k study uses 6 'typical' weeks of the year and extends it to the whole year, while the data provided in [**24**] contain the real movements for every single day of the year 2006.

However some differences may appear between the data obtained from the AERO2k study and [**24**], using homogeneous data is essential before drawing any conclusions concerning the comparison between LTO flights and overflights and this is certainly what's happening in the Belgian context of the ABCI project as the homogeneous and exhaustive data from Belgocontrol will continue to be processed in the coming months.

B.2 Climate impacts

To give an estimation of the impact on climate it was decided to relay on radiative forcing, as figures for the global radiative forcing are published whereas the impact on temperature and other climate indicators are not available for all of the impacts considered.

The impact of ozone on surface temperature for the global and the European domain was taken from [**7**]. These results were compared with the RF of ozone given by [**33**] and transformed into RF:

$$RF_{\mathrm{O_3,EU}} = \frac{RF_{\mathrm{O_3,glo}}}{T_{\mathrm{O_3,glo}}} T_{\mathrm{O_3,EU}},$$

where $RF_{\mathrm{O_3,X}}$ indicates the radiative forcing averaged on region X, and $T_{\mathrm{O_3,X}}$ is the temperature increase due to changes in ozone concentration.

The impact of ozone in Belgium and in Europe in general was supposed to be the same as ozone is more or less evenly distributed on the regional but not on the global level [**1**]. The distinction between LTO traffic in the region and the overflights was then made proportional to the NO_x emitted. This calculation does not take into account the influence of the flight altitude on ozone impacts, as the available data did not permit such a calculation.

The global RF for contrails and aircraft induced cloudiness are taken from [**15**] and are scaled following the fuel use above FL240, as aircraft flying below this level do not form contrails. The radiative forcing averaged over Europe or Belgium is stimates as:

$$RF_{\mathrm{cont/AIC,EU/BE}} = \frac{FuelUse_{\mathrm{EU/BE,FL>240}}}{FuelUse_{\mathrm{glo,FL>240}}} \frac{Surface_{glo}}{Surface_{EU/BE}} RF_{\mathrm{cont/AIC,glo}},$$

where $RF_{\mathrm{cont/AIC,X}}$ is the radiative forcing for contrails or AIC averaged over region X, $FuelUse_{\mathrm{X,FL>240}}$ is the fuel used by planes above region X and above FL240(which corresponds to $24,000$ft (≈ 8000m)) and $Surface_X$ represents the surface of the region X considered. The $RF_{\mathrm{cont/AIC,glo}}$ is taken from [**15**] and $FuelUse_{\mathrm{X,FL>240}}$ is determined using the AERO2k database (see [**6**]) and data from [**24**] for the flights over Belgium.

However these results do not take into account the fact that average meteorological conditions over Europe are different from the average conditions on a global scale. For a future more detailed comparison the conditions when contrails are formed and the supersaturation needed to take into account the persistence of contrails are different, which can be done using a regional climate model.

ANNEX C
WORK REPORT

This annex gives first the lectures attended during the last academic year as well as the summer school, scientific meetings and workshops attended.

C.1 Lectures attended

Lectures attended with an evaluation at the end of the lecture:

ENVI3006 Droit de l'environnement

PHYS3150 Questions spéciales de modélisation du système climatique

PHYS3255 Séminaire de climatologie physique et de géophysique

SPED3300 Societés, populations, environnement, développement : problématiques et approches interdisciplinaires

The following lectures were attended but no evaluation at the end of the lecture was made (cours suivis en tant qu'étudiant libre):

FYQU3038 Sea ice and icebergs in the clim.syst.

MECA2600 Introduction au génie nucléaire et théorie des réacteurs I

PHYS3160 Physique de l'atmosphère à la micro et méso-échelle

C.2 Summer schools, scientific meetings and workshops

Summer school attended:

- International Summer School "Aviation Weather and the Atmopshere" in Braunschweig (Germany) (21st august until the 1st september 2006)
- Ateliers de Modélisation Atmosphérique (AMA2007) : Paramétrisations physiques des processus atmosphériques et de surface in Toulouse (France) (16th until the 18th january 2007)

The summer school of the european QUANTIFY project[29], which takes place from the 9th september to the 26th september 2007 will be attended.

Selection of scientific meetings and workshops attended:

- IPPC WGII Plenary in Brussels as observer of the Belgian delegation from the 2nd april to the 6th April 200t. Comments on the synthesis report of the fourth assessment report of the IPCC, to be approved in November 2007 have been submitted.
- Working groups organized by the European Commission about the introduction of the aviation sector in the EU-ETS (7th june) and about the European 2° target (28th june).
- Regular (once a month) meetings of the ABCI members, where scientific insights and fundamental questions of the project are discussed as well as stakeholder meetings of the ABCI project, where presentations about the key scientific findings were made.
- Participation in some of the internal meetings as well as the stakeholder meetings of the *"ad hoc committee on bunker fuels – aviation and EU-ETS" of the national Coordination Committee International Environmental Policies (CCIEP) – Greenhouse Effect*

[29]European project aiming to quantify the impact of aviation on climate, see http://www.pa.op.dlr.de/quantify/

LIST OF SYMBOLS

$\beta(\mu_0)$	Mean fractional upward-scattering coefficient for primary scattered solar radiation
β_0	Mean fractional backscattering coefficient for diffuse light
χ	Total mass of ice particles in a considered volume
Δt	Time step of the model
δ'	Optical thickness
$\Delta_n z$	Pathlength
η	Aircraft overall efficiency
Γ	The gamma function
μ_0	Cosine of solar zenithal angle
ρ	Density of the air
ρ_i	Density of ice particle
ρ_l	Type density of the liquid particles
$\mathrm{EI}(\mathrm{H_2O})$	Emission index of water vapor
$\tilde{\omega}'$	Single scattering albedo
B	Blackbody radiation
c_D	Viscosity coefficient
c_p	Specific heat capacity of air
C_{pd}	Specific heat of dry air at constant pressure
clc	Subgrid cloudiness
d_v	Diffusion coefficient for water vapor
D_x	Particle x with diameter D
D_{wa}	Diffusivity of water vapor in dry air
E_1	Efficiency factor an gives the probability of collision between the particles

E_2	Factor of coalescence that gives the probability that a particle that two particles entering into collision stay effectively together
f	Fraction of radiation contained in the diffraction peakoff the phase function
F_1, F_2	Diffuse upward, downward flux
g	Acceleration of gravity
g^λ	Asymmetry factor for the phase function
h	Planck constant
H_i	Howell factor
h_i	Thickness of hexagonal ice crystals
J	Number of ice crystals that are formed in a unit of volume during a second
k	Stefan-Botzmann constant
k^λ	Droplet absorption or scattering coefficient at wavelength λ
k_h	Thermal conductivity of air
l_h	thermal conductivity of dry air
L_s	Latent heat of vaporization
L_s	Latent heat of evaporation
M	Mass of a drop
N_i	Number of cloud ice particles par unit volume of air
n_s	Distribution of active freezing nuclei
n_{D_x}	number of particle x that have a diameter D
p	Air pressure
Q	Combustion heat
q^c	Mass fraction of cloud water
q^i	Mass fraction of ice crystals
q^v_{si}	Saturation specific humidity with respect to ice
q^v_{sw}	Saturation specific humidity with respect to water
q_l	Cloud water content
q_r	Concentration of rain drops in a unit volume of air
q_s	Saturation humidity in the grid cell
q_t	Total water content of the air
q_v	Average water vapor in one grid cell of the atmosphere

R	Radius of a drop
R_d	Gas constant for dry air
R_v	Gas constant of water vapor
S	Supersaturation ratio
S^c_{frz}	Rate of homogeneous nucleation
S^i_{dep}	Total deposition rate of ice crystals
S^λ_0	solar irradiance at the top of the atmosphere at wavelength λ
S_{agg}	Ration of aggregation process of ice crystals
S_{au}	Ratio of autoconversion process of ice crystals
S_{berg}	Ratio related to Bergeron process
S_{final}	Ratio of heterogeneous nucleation
S_{icesub}	Ratio related to sublimation process
S_{nuc}	Ratio related to nucleation process
T	Mean temperature of grid cell
T_0	Freezing point temperature of water
T_l	Liquid water temperature
U	Diffusivity factor
U_T	Terminal velocity of ice particle
w_n	Weighting factors
${\tau_n}^\lambda$	Transmission through a pathlength
ABCI	Aviation and the Belgian Climate Policy project : Analysis of Integration Options and Impact, belgian project funded by the Belgian Science Policy
AIC	Aircraft Induced Cloudiness
AIRS	Atmospheric Infrared Sounder on the NASA Aqua spacecraft
CCOPE	Cooperative Convection Precipitation Experiment
CEPEX	Central Equatorial Pacific Experiment
CLM	Regional climate model, derived from the 'Lokal Modell', developed by the DWD
CPU	Central Processing Unit
CRF	Cloud Radiative Forcing
DWD	'Deutscher Wetterdienst', german meteorological office

EUCREX	European Cloud and radiation experiment
FIRE I/II	First/second International Satellite Cloud and Climatological Project (ISCCP) Regional Experiments
FL	Flight Level
GCM	General circulation models, used to do climate runs on the global scale
ICE	International Cirrus Experiment
JECK	In situ measurements made by aircrafts over the United states from 1979 to 1984
KWAJALEIN	In situ measurements of cloud properties over the Kwajalein island in the Pacific
LTO	Landing and takeoff
MEA	Mean Absolute Error
NASA	National Aeronautics and Space Administration
NCEP	National Centers for Environmental Prediction
RF	Radiative Forcing
RH	Relative humidity
SUCCESS	Subsonic Aircraft: Contrail and Cloud Effects Special Study
TERRA_ML	Soil model used in the CLM

BIBLIOGRAPHY

[1] T. K. Berntsen, M. Gauss, I. S. A. Isaksen, V. Grewe, R. Sausen, G. Pitari, E. Mansini, E. Meijer, and D. Hauglustaine. Sources of nox at cruise altitudes: Implications for predictions of ozone and methane perturbations due to nox from aircraft. *Proceddings of the AAC-Conference, June30 to July 3, 2003, Fridrichshafen, Germany*, pages 190–196, 2003.

[2] H. C. Davies. A lateral boundary formulation for multi-level prediction models. *Quarterly Journal of the Royal Meteorological Society*, 102:405–418, April 1976.

[3] Eurocontrol. Atm contrail mitigiation options environmental study. *Eurocontrol*, 2005.

[4] Eurocontrol. Medium-term forecast flight movements 2006-2012 voume1, February 2006.

[5] Eurocontrol. Trends in air traffic volume 1, getting to the point: Business aviation in europe. Eurocontrol, May 2006.

[6] C.J. Eyers, P. Norman, J. Middel, M. Plohr, S. Michot, and K. Atkinson. *AERO2k Global Aviation Emissions Inventories for* 2002 *and* 2025, 2004.

[7] A. Ferrone. Modeling the impact of aviation on climate. Master's thesis, Universté catholique de Louvain, 2006.

[8] N. H. Fletcher. *Physics of rain clous*. Cambridge University Press, London, 1962.

[9] J.-F. Geleyn and A. Hollingsworth. An economical analytical method for the computation of the interaction between scattering and line absorption of radiation. *Beitr Phys Atmos*, 52:1–16, 1979.

[10] A. Gettelman, W. D. Collins, E. J. Fetzer, A. Eldering, F. Irion, W. P. B. Duffy, and G. Bala. Climatology of upper tropospheric relative humidity from the atmospheric infrared sounder and implications for climate. *J.Climate*, 19(23):6104–6121, 2006.

[11] A. J. Heymsfield and L. Miloshevish. Relative humidity and temperature influences on cirrus formation and eveolution: observations from wave clouds and fire ii. *Journal of Atmospheric Sciences*, 52:4302 – 4326, 1995.

[12] A. J. Heymsfield and C. M. R. Platt. A parametrization of the particle size spectrum of ice clouds in terms of ambient temperature and their ice water content. *Journal of Atmospheric Sciences*, 41:864 – 855, 1984.

[13] P. V. Hobbs and A. L. Rangno. Ice particle concentrations in clouds. *Journal of Atmospheric Sciences*, 42:2523–2549, December 1985.

[14] IPCC, Joyce E. Penner, David H. Lister, David J. Griggs, David J. Dokken, and Mack McFarland, editors. *Aviation and the Global Atmosphere*. Cambridge University Press, Cambridge, United Kingdom and New York, NY, USA, 1999.

[15] IPCC, S. Solomon, D. Qin, M. Manning, Z. Chen, M. Marquis, K.B. Averyt, M. Tignor, and H.L. Miller, editors. *Climate Change 2007: The Physical Science Basis. Contribution of Working Group I to the Fourth Assessment Report of the Intergovernmental Panel on Climate Change*. Cambridge University Press, Cambridge, United Kingdom and New York, NY, USA, 2007.

[16] A. Khain, M. Ovtchinnikov, M. Pinsky, A. Pokrovsky, and H. Krugliak. Notes on the state-of-the-art numerical modeling of cloud microphysics. *Journal of Climate*, 14:900–919, 2001.

[17] N. C. Knight. The climatology of hailstone embryos. *Journal of Applied Meteorology*, 20:750–755, July 1981.

[18] L. R. Koenig. Numerical modeling of ice deposition. *Journal of the Atmospheric Sciences*, 28(2):226–237, 1971.

[19] C. Krupp. Holographische messungen an eiskristallen in cirruswolken während des internationalen cirrus experiments (ice). *GKSS*, 92/E/14, 1992.

[20] L Lekov, B Rockel, H Kapitza, and E Raschke. 3d mesoscale numerical studies of cirrus and stratus clouds by their time and space evolution. *Contributions to Atmospheric Physics/Beitraege zur Physik der Atmosphaere.*, 65(1):35–57, Feb 1992.

[21] J. Y. Liu and Orville H. D. Numerical modeling of precipitation effects on cumulus cloud. *Inst. Atmos. Sci.*, 68-9:70, 1968.

[22] J.-F. Louis. A parametric model of vertical eddy fluxes in the atmosphere. *Boundary-Layer Meteorology*, 17:187–202, September 1979.

[23] D. K. Lynch, K. Sassen, D. O'C. Starr, and G. Stephens, editors. *Cirrus*. Ofxford Universtiy Press, 2002.

[24] J. Matheys, T. Festraets, J. Van Mierlo, C. Macharis, N. Sergeant, and J.-M. Timmermans. Aviation and climate change: a comparison of the overflights of the belgian territory and the local aviation activities. *to be published*, 2007.

[25] M. P. Meyers, P. J. Demott, and W. R. Cotton. New primary ice-nucleation parameterizations in an explicit cloud model. *Journal of Applied Meteorology*, 31:708–721, July 1992.

[26] P. Personne, C. Duroure, C. Isaka, and H. Isaka. Geometrical charcterisatics of cirrus ice crystals. *Internation assocation of Meterological and Atmopsheric Physics*, program and Abstracts(IAMAP):Villeneuce d'Ascq, France, 1991.

[27] M. Ponater, S. Marquart, and R. Sausen. Contrails in a comprehensive global climate model: Parameterization and radiative forcing results. *Journal of Geophysical Research (Atmospheres)*, 107:2–1, July 2002.

[28] H. R. Pruppacher and J. D. Klett. *Microphysics of Clouds and Precipitation*. Johannes Gutenberg University, New Mexico State University, 1997.

[29] E. Raschke, P. Flamment, Y. Fouquart, P. Hignett, H. Isaja, P. R. Jonas, and Sundquiat H. Cloud-radiation sutdies during the european cloud and radiation experiment (eucrex). *Survey Geophys*, 14:89 – 138, 1998.

[30] H. Raschke, J. Schmetz, J. Heintzenberg, R. Kandel, and R. Saunders. Internation cirrus experiment. *ESA Bull.*, 14:113–119, 1990.

[31] Bodo Ritter and Jean-Francois Geleyn. A comprehensive radiation scheme for numerical weather prediction models with potential applications in climate simulations. *Monthly Weather Review*, 120(2):303–325, 1992.

[32] R. Sausen, K. Gierens, M. Ponater, and U. Schumann. A Diagnostic Study of the Global Distribution of Contrails Part I: Present Day Climate. *Theoretical and Applied Climatology*, 61:127–141, 1998.

[33] R. Sausen, I. Isaksen, V. Grewe, D. Hauglustaine, D. Lee, G. Myhre, M.O. Köhler, G. Pitari, U. Schumann, F. Stordal, and C. Zerefos. Aviation radiative forcing in 2000: An update on ipcc (1999). *Meteorol. Z.*, 14:555 – 561, 2005.

[34] G. L. Stephens. Optical properties of eight water cloud types. Technical report, CISRO, Division of Atmosperic Physics, 1979.

[35] M. Tiedtke. A comprehensive mass flux scheme for cumulus parameterization in large-scale models. *Mon. Wea. Rev.*, 117:1779–1800, 1989.

[36] W. J. Wiscombe and G. W. Grams. The backscattered fraction in two-stream approximations. *Journal of Atmospheric Sciences*, 33:2440–2451, 1976.

[37] W. G. Zdunkowski and G. J. Korb. Numerische methoden zur lösung der strahlungsübertragungsgleichung. *PROMET*, 2/3:26–39, 1985.